Effective soil-stiffness validation

Shaker excitation of an in-situ monopile foundation

Versteijlen, W. G.; Renting, F. W.; van der Valk, P. L.C.; Bongers, J.; van Dalen, K.N.; Metrikine, A. V.

DOI
10.1016/j.soildyn.2017.08.003

Publication date
2017

Document Version
Accepted author manuscript

Published in
Soil Dynamics and Earthquake Engineering

Effective Soil-Stiffness Validation: Shaker Excitation of an In-Situ Monopile Foundation

W.G. Versteijlen[a,b], F.W. Renting[b], P.L.C. van der Valk[a], J. Bongers[a], K.N. van Dalen[b], A.V. Metrikine[b]

[a] *Siemens Wind Power, Beatrixlaan 800, 2595 BN Den Haag, The Netherlands*
[b] *Faculty of Civil Engineering and Geosciences, Delft University of Technology, Stevinweg 1, 2628CN Delft, The Netherlands*

Abstract

In an attempt to decrease the modelling uncertainty associated with the soil-structure interaction of large-diameter monopile foundations, a hydraulic shaker was used to excite a real-sized, in-situ monopile foundation in stiff, sandy soil in a near-shore wind farm. The response in terms of natural frequency and damping of a pile-only system is significantly more influenced by the soil than a full offshore wind turbine structure, and therefore ensures a higher degree of certainty regarding the assessment of the soil reaction. Steady-state vibration amplitudes with frequencies between 1 and 9 Hz were retrieved from strain gauges vertically spaced along the embedded pile, and accelerometers attached to the top of the pile and to the shaker. The measured response is used to validate an effective 1D stiffness method, which is applied as a smart initial guess for a model-based identification of the effective soil-structure interaction properties in terms of stiffness, damping and soil inertia. The performance of the stiffness method is compared to the currently employed p-y stiffness design method. While the effective stiffness method seems to overestimate the actual low-frequency stiffness with about 20%, the p-y method appears to underestimate this stiffness with 140%. The assumption of linear soil behaviour for most of the occurring pile displacements is shown to be acceptable. A damping ratio of 20% (critical) is identified as effective soil damping for the monopile, which is estimated to correspond to a 0.14% damping ratio contribution from the soil for the full structure. The unique measurement setup yielded a 'first-off' oppor-

tunity to validate a soil-structure interaction model for a rigidly behaving pile. We have shown that indeed such a pile reacts stiffer than predicted by the *p-y* curve method, and that its response can be modelled more accurately with our recently developed effective stiffness method.

Keywords: shaker excitation, soil-structure interaction, rigid monopiles, resonance, frequency-dependent effective soil stiffness, in-situ validation, offshore wind foundations, soil damping

---

1. Introduction

Some uncertainties exist in the current structural design parameter estimation of large-diameter monopile (MP) foundations for offshore wind turbines (OWTs). These are mainly related to properties of the wave loading and the dynamic interaction between the pile and the soil it is embedded in. Focussing on the dynamic soil-structure interaction (SSI) for OWT monopile foundations, the main uncertainties are related to the quantification of the small-strain stiffness and damping in this system. The magnitude of both these parameters are believed to be underestimated in the current design practice. A proper estimation of the stiffness is a prerequisite for the correct prediction of the fundamental natural frequency of the OWT, being a key design parameter in aiming to limit resonance with wave and blade-passing frequencies. For most installed OWTs the fundamental frequency (of the first bending mode of the support structure) is substantially higher than aimed for in design [1], and this discrepancy is often attributed to incorrect modelling of the effective soil stiffness. The most often used stiffness model is based on the p-y curve method developed in the 1960s - 1980s by, amongst others, Reese [2], Matlock [3] and O'Neill [4]. This method provides a Winkler foundation-based nonlinear stiffness profile consisting of uncoupled discrete springs. The input for this method consists of geotechnical soil parameters that can be retrieved from, for instance, the Cone Penetration Test (CPT). Besides the fact that these 'p-y springs' were never intended to facilitate the description of the dynamic behaviour of piles (but rather static or cyclic, larger-strain behaviour), they were calibrated on long flexible piles with a large ratio of embedded length to diameter (L/D ratio>20). Most MPs used in the offshore wind industry nowadays have L/D ratios smaller than 7, which causes these piles to bend and shear in a more rigid way [5]. The increased effect of soil reaction mechanisms like base-shear forces [6] - [8] and global (coupled) soil reactions towards rigidly behaving piles, make the response of these piles deviate from that of flexible piles.

Current designs of the OWT foundations are often fatigue-driven, and are therefore greatly benefited by a realistic estimation of the damping. Besides aerodynamic damping, the largest damping contribution is believed to stem from the soil. However, both the identification and the modelling of the damping is challenging and rather uncertain. Most published attempts on modal identification, [9] - [16], find values larger than assumed in the original design models of the OWTs, which is often around 1% of critical support structure damping (excluding aerodynamic damping).

Extensive work has been performed on dynamic SSI modelling over the past decades. The engineering models [17, 18] as well as the extensive 2D and 3D solutions, [19] - [21], however, all have in common that they were mainly focussed on describing the SSI of slender, flexible piles and therefore the engineering methods and tables, as in some of these cited papers, linking stiffness and damping coefficients to soil and structure type need to be updated for OWT foundation dimensions and typical frequencies. This can be (partially) fulfilled using today's possibilities in numerical and semi-analytical solution methods (Finite Element methods, Boundary Element method, etc) by building extensive SSI models [22, 23], and using those to tune the coefficients of simpler engineering models [24]. However, the question still remains how to quantify the input parameters of those extensive SSI models.

Measuring the in-situ soil properties that define the dynamic SSI is a challenging task. Controlled laboratory tests on retrieved borehole samples might not be fit for this because of the dual reason that (a) the samples will always be disturbed when extracted from the soil, and it is challenging to re-simulate in-situ conditions, and (b) when the dynamic properties of these samples will be tested at the low frequency of interest ($\backsim$ 0.3 Hz), the typical wavelengths will be in the order of a few hundreds of meters, making the response prone to boundary disturbances. Therefore we have advocated the use of in-situ seismic measurements [25]. Clearly, once we find proper ways of characterizing the soil

properties, and use those properties in adequate dynamic SSI models, the loop has to be closed by performing validation measurements on full-scale in-situ MPs.

Only few publications are available on controlled ('known input') dynamic testing of laterally loaded, in-situ, rigidly behaving MPs. The few available attempts of using a shaker as excitation source were on very slender piles in on-shore conditions [26, 27] or on an onshore wind turbine which is not supported by a MP [28]. Research on lateral pile-resistance has been performed by Byrne et al. [29]. Based on the limited information available at the time of writing, it appears that these experiments mainly focused on monotonic (static) loading, and that in a lesser extend also one-way cyclic loading was applied. Piles varying from 0.27 m to 2 m in diameter were tested at two onshore sites (one with mainly clay, the other sand). By also varying the embedded length, L/D ratios were obtained that are characteristic for current MP foundations.

In this contribution we present the in-situ, controlled dynamic excitation tests that were performed on a full-scale, stand-alone monopile foundation of an offshore wind turbine in a near-shore farm. As our research challenges lie in the dynamic SSI (small-strain harmonic, not cyclic), controlled dynamic excitation is desired. Testing a real MP allows to - besides including realistic geometric, soil saturation and pile installation effects - link the identified SSI characteristics to subsequent response of a complete operational OWT. Due to the high sensitivity of a stand-alone MP to the soil, this setup offers the highest degree of certainty for validating a SSI model, as opposed to using the structural response of the full OWT. This led us to design a test setup described in Section 4, on a site where we performed extensive soil-characterization measurements, of which the output is given in Section 2. Of the two tested MPs, one pile is fully equipped with strain gauges and sensors in the soil, and is therefore the pile discussed in this paper. In the model-based identification (Section 5) of the SSI properties in terms of stiffness, damping and possible inertia effects,

we aim to match measured transfer and transmissibility functions with modelled counterparts using a 1D model and 2 modifications of that model. We use our previously developed effective stiffness method - based on seismic measurements and 3D modelling [30] - to calculate the in-situ 1D stiffness $k_{_{eff}}(z)$, which is equivalent to the modulus of horizontal subgrade reaction [31]. $k_{_{eff}}(z)$ is used as a starting point for the identification, and we check (validate) how well it performs in comparison with the often used *p-y* stiffness method; the mismatch between the modelled and measured pile response is quantified for both methods. In Section 5.2 we discuss the three observed frequency regimes, the damping and natural frequency of the full OWT structure, and we reflect on the linear-soil assumption. Finally, the main conclusions are given in Section 6.

2. Site Characterization

The shaker tests were performed on monopiles of the Westermeerwind wind farm - a near-shore farm in The Netherlands, situated at the East side of the IJsselmeer lake, see Figure 1. The saturated soil conditions being quite similar to sandy North Sea sites in combination with the limited water depth of 4-5 m and good accessibility, make it an appropriate location for the experimental investigation of soil-structure interaction. Besides CPTs and the retrieval of borehole samples, also geophysical measurements in the form of the Seismic Cone Penetration Test (SCPT) were incorporated in the soil investigations (performed by Fugro in 2012), in order to characterize the small-strain behaviour of the soils.

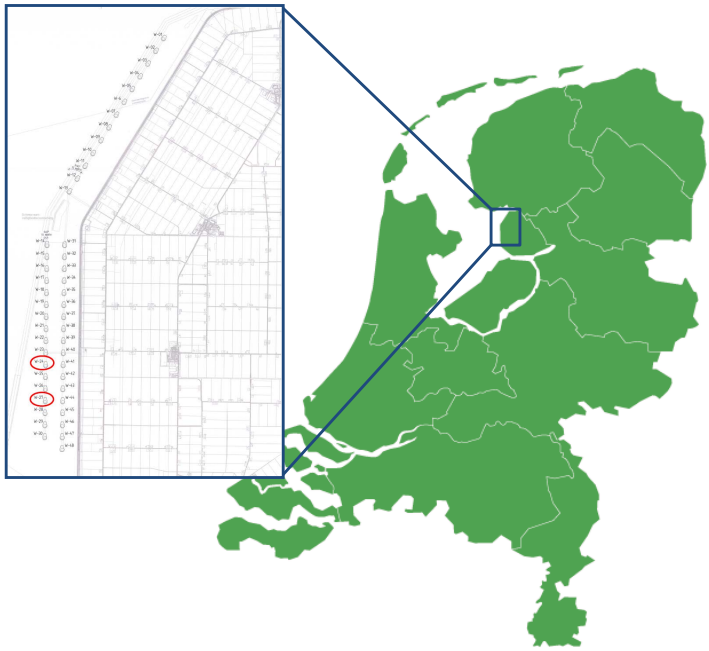

Figure 1: Location of Westermeerwind wind farm. The red circles indicate the shaker testing locations, named 'W24' and 'W27' (southernmost position of the two).

This section only presents the resulting parameter profiles from the geotechnical and geophysical characterization. More explanation on the geophysical characterization is given in Appendix A. The in-situ density ρ and the effective angle of internal friction φ' for location W27 - the testing location of the experiments described in this paper - are shown in the left and right panel of Figure 2, respectively. The estimated Poisson's profile and computed Young's modulus for location W27 are given in Figure 3. The elastic continuum parameters (Young's modulus, density and Poisson's ratio) are input for a 3D soil-pile model which is discussed in the next section. The internal friction angle is given as a reference, as it is an important input parameter for the p-y curve method.

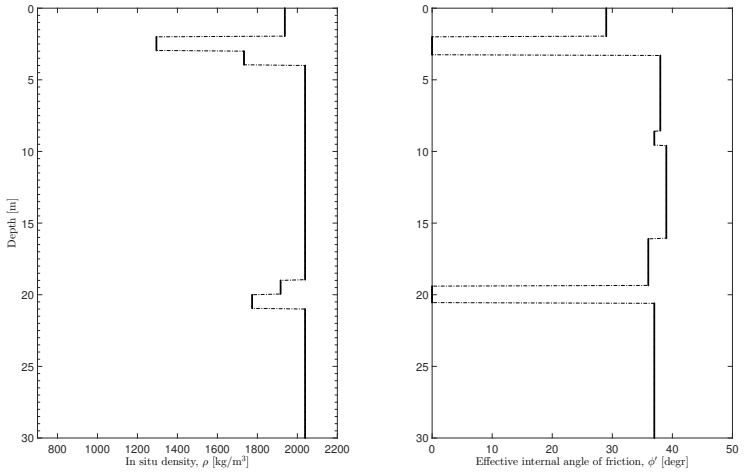

Figure 2: In-situ density ρ (left panel) and effective angle of internal friction φ' (right panel) of location W27. The mean values of the in-situ density of the different soil types and layers encountered in the farm were determined based on unit weight, water content, oedometer and triaxial tests. The angle of internal friction was estimated using the correlation with the relative density according to Jamiolkowski [32], as prescribed by the standards [33], and validated with the output of triaxial tests. For the layers classified as cohesive material, φ' is set to zero.

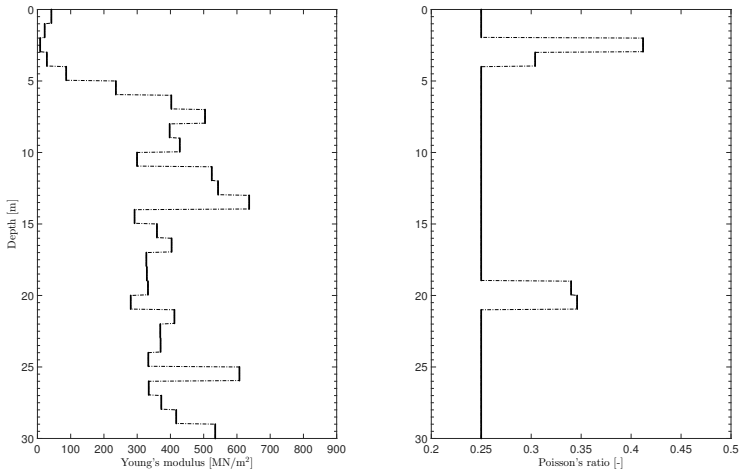

Figure 3: The Young's modulus profile (left panel) and Poisson's ratio profile (right panel) are input for the 3D linear elastic model for location W27.

3. 3D and 1D effective stiffness

The derived elastic continuum parameters are input for the effective stiffness method [30], of which we here only present the resulting effective 1D stiffness profile capturing the 3D small-strain stiffness of the interacting pile and soil.

Using the continuum parameters of figures 2 and 3, a horizontally stratified model of the soil was built with ANSYS software, employing linear elastic solid elements (similar to those employed in [25]). The tested pile has an embedded length of 24 m and a diameter of 5 m. The wall thickness of the pile is 50 mm, except for the top and tip region where it has been thickened to 60 mm for pile-driving requirements. The pile was modeled using shell elements, assuming a constant wall thickness of 50 mm over the entire length of the pile. The element size for the pile and the soil close to the pile was set to 0.25 m, and the soil elements were attached to those of the pile (i.e. neither slip nor gap formation). The total depth of the soil medium was set to 50 m, and the halfspace was given a radius of 40 times the radius of the pile; i.e., 100 m. These dimensions of the model were found to be large enough in order for the boundaries of the model not to influence the deflections of the pile. The horizontal layers were given a 1 m thickness up to 30 m depth (which is the depth up to which the shear modulus was identified), and the lowest layer from 30 m to 50 m depth was given the same properties as the lowest identified layer (from 29 to 30 m depth, see Figures 2 and 3).

A static horizontal force was applied to the top of the MP which extends 9.85 m above mudline. The obtained pile displacements and rotations were used in the method presented in [30] for translating the 3D results into a 1D effective stiffness profile. The resulting effective stiffness $k_{_{eff}}(z)$ is shown in Figure 4. This stiffness is comparable to (has the same application and unit as) the initial horizontal subgrade modulus, in the p-y curve formulation often called $k_{s,0}$ or E^*_{py}, [MN/m^2]. For comparison, the p-y curve initial stiffness is also shown

in Figure 4. Note that the effective stiffness $k_{eff}(z)$ is a true SSI-parameter; it incorporates both the geometry of the pile, the properties of the soil and the properties of their interface. The shape of this profile can therefore not be one-to-one related to the shape of profiles of (pure) soil-stiffness parameters. The match in displacements, slopes, rotations and curvatures (bending) of a Timoshenko beam supported by the effective stiffness profile of Figure 4 and those of the 3D model is shown in Figure 5. Although the fit in terms of curvature can be improved (the effective 1D stiffness seems somewhat stiffer than the 3D stiffness), the match is satisfactory. As a reference, the responses of a 1D model with the *p-y* stiffness profile is also included (light grey dashed lines). The (static) effective stiffness profile of Figure 4 will be used as an initial guess in a model-based analysis of the shaker measurements (Section 5).

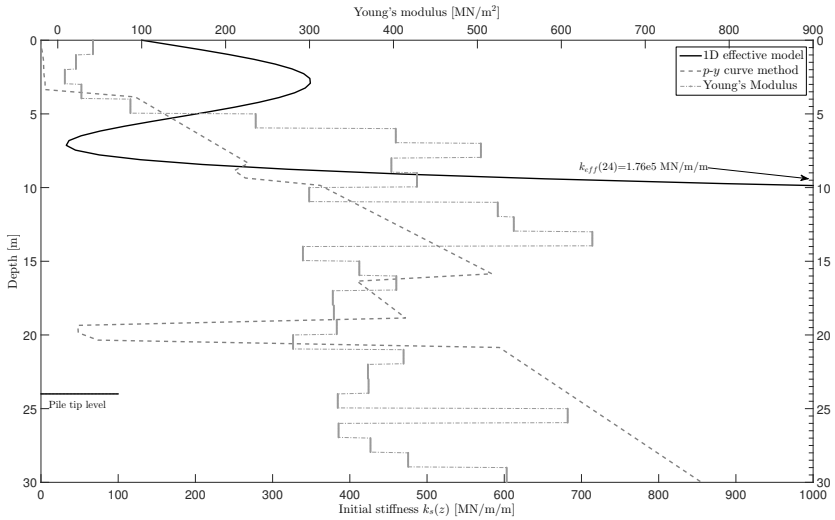

Figure 4: The effective $k_{eff}(z)$ (black solid line). This initial stiffness incorporates 3D modelling effects and small-strain elastic properties of the soil obtained using in-situ seismic measurements. As a reference, the *p-y* curve initial stiffness is given by the grey dashed line. The Youngs profile which was input for the 3D model, is included as a reference (grey dashed-dotted line).

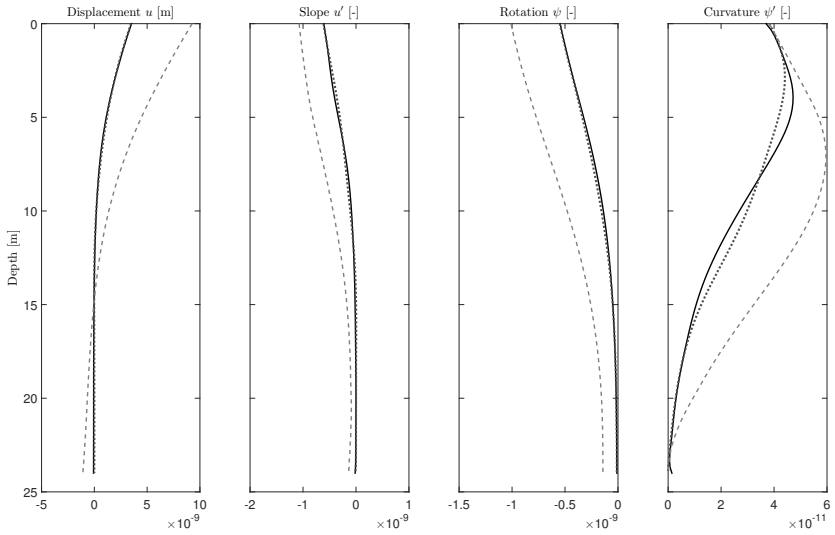

Figure 5: The displacement, slope, rotation and curvature of a 1D Timoshenko beam supported by the effective Winkler profile (Figure 4), compared with the original 3D linear elastic model. As a reference, these 4 quantities for a Timoshenko beam supported by the initial stiffness derived by the p-y curve method are displayed by the grey dashed line. The 3D model was loaded with a horizontal force of 1 N, and overturning moment of 9.85 Nm. The 1D beam models were loaded with double this loading (2 N and 19.70 Nm) since only half of the symmetric problem was simulated in the 3D model.

4. Measurement setup & data pre-processing

Figure 6 shows the measurement setup for pile W27: 7 rings of strain gauges are attached to the inner pile wall, with 6 rings below, and 1 ring just above mudline. Each ring contains 4 strain gauges: one for each quadrant. The rings are vertically distributed, with a concentration around the location where most bending was expected to occur. Besides standard protection covers for the strain gauges, fibreglass reinforced composite cable trays were glued on the pile-wall to guide and protect the cables. Steel wedges were welded on the pile near the pile tip to protect the lower edges of the cable trays during installation of the pile. During this installation, 7 strain gauges were damaged: the lowest ring of strain gauges and three strain gauges of rings no. 3, 4 and 6 (see Figure

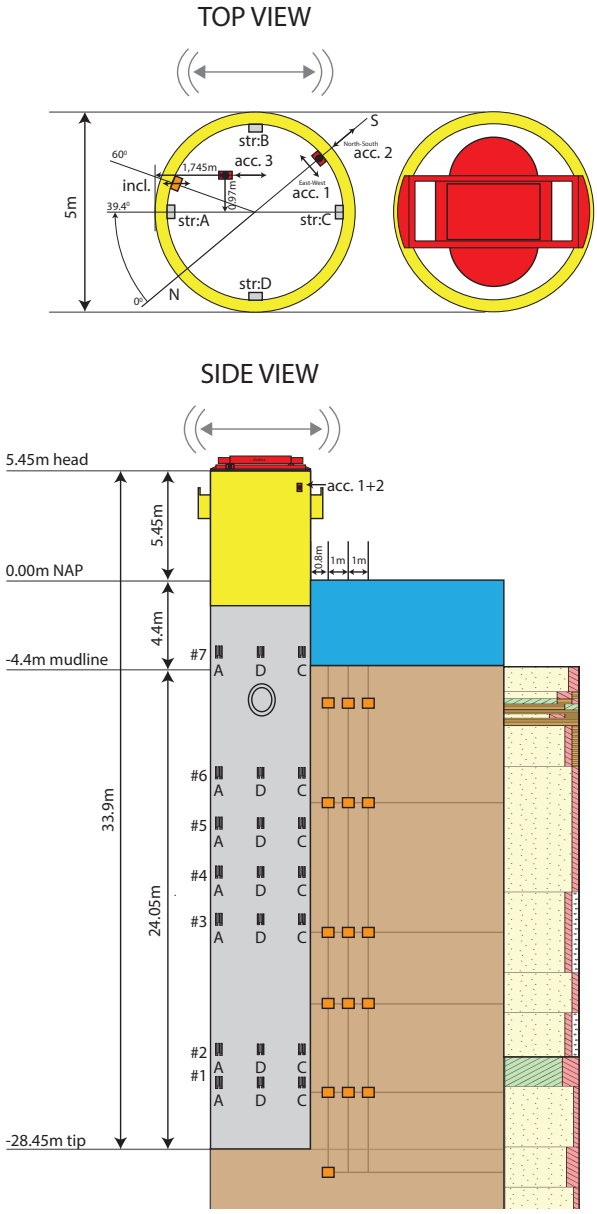

Figure 6: Measurement setup for pile W27. Side view: the vertical levels are in relation to NAP (Dutch equivalent of Mean Sea Level). The orange boxes indicate the positions of the cones equipped with accelerometers and pore water pressure meters. The hatched spots on the pile (named A-D-C) indicate the position of the strain gauges, with their ring number indicated at the left side of the pile. The cable entry hole is indicated below strain gauge D7. A borehole classification of the soil is given in the right part of the figure, with yellow indicating sand, green for clay and brown for peat, see Figure A.2.

6) on the axis perpendicular to the shaker-loading direction. Furthermore, 2 Althen AAA320 accelerometers were attached to the inner pile wall at the top of the pile for measuring the pile accelerations in North-South and East-West direction. The company HBM installed all pile-related sensors and provided the data acquisition system.

To monitor the soil-structure interaction during dynamic excitation of the MP, the reaction of the soil and of the pile were synchronically measured. To this end, 16 cones with accelerometers and piezometers were placed at various depths and radial distances from the pile. The data retrieved from these soil sensors will, however, not be discussed in this paper.

As can be seen in the right panel of Figure 7, the shaker consists of 2 large cogwheels (ensuring synchronization) that are hydraulically powered. On top of these cogwheels, multiple steel plates with various weights can be attached at different radii from the center of the cogwheel. An artist impression of the shaker is given in the left panel of Figure 7. The shaker can deliver a maximum hydraulic power of 50 kW, rotate at a maximum frequency of 8.6 Hz and was designed to not supersede an excitation force of 160 kN. The total weight of the shaker (excluding ballast plates, including frame) is 4500 kg. An accelerometer was attached to the shaker frame, and a tachometer measured the rotational velocity of the cogwheels. All sensors were sampled with a frequency of 600 Hz.

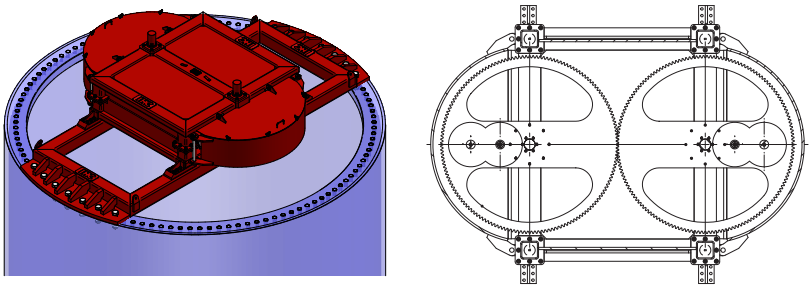

Figure 7: Artist impression of the shaker on the monopile (left panel) and top-view drawing of the shaker, showing the cogwheels that ensure synchronized revolution of the masses (right panel).

Figure 8 shows an aerial photo of the mobilized barges and crane that were used for performing the measurements.

Figure 8: Aerial photo showing the shaker on pile W27, the mobilized barges and crane.

Three weight setups were used for exciting the monopile:

- Heavy weight: 10 plates of 20.5kg on each cogwheel = 410kg
- Middle weight: 3 plates of 20.5kg on each cogwheel = 123kg

- Light weight: 1 plate of 20.5kg on each cogwheel = 41kg

The shaker was calibrated in a test centre by connecting it to a rigid frame which was placed on a large-mass concrete foundation slab. An extensive study was performed on the recorded data from the different force transducers that were placed between the shaker and the rigid frame [34]. This study determined an effective arm R for the different setups, which can be used to compute the centrifugal force amplitude:

$$F = m\omega^2 R. \tag{1}$$

Here ω is the angular frequency at which the mass m of the shaker is rotating. The products of the effective arm and mass for the 3 setups (including for instance the mass of spacer rings used to install the plates and manufacturing imperfections) can be found in Table 1. The table also lists the considered frequency ranges of excitation and the associated maximum and minimum forces as applied on the MP. Finally, for later use (Section 5.1.1), also the force ratio between the setups for excitation at equal frequency is given.

	Arm x mass [mkg]	Force ratio [-]	Performed freq. range [Hz]	Min. force [kN]	Max. force [kN]
Heavy weight	239.32	1	1.04 - 4.03	10.31	153.42
Middle weight	88.76	0.37	1.06 - 6.70	3.95	157.31
Light weight	32.08	0.13	5.04 - 8.68	32.15	95.40

Table 1: Conducted tests analyzed in this paper

Three types of tests were conducted with the shaker: a constant frequency sweep (constant increase of ω), a step-wise increase of the frequency aimed at creating steady-state conditions during the constant-frequency plateaus, and an emergency stop aimed at decay tests. Unfortunately, the decay data seems to indicate that the motions of the MP were damped out faster than the time it took for the shaker to come to a standstill, making it challenging to analyze this data. This paper only considers the step-wise tests, in which we assume that steady-state conditions of the system have been reached. Figure 9 gives an example time trace of the revolutions per second (RPS) of the tachometer

recording during the step-wise test with the Middle weight setup.

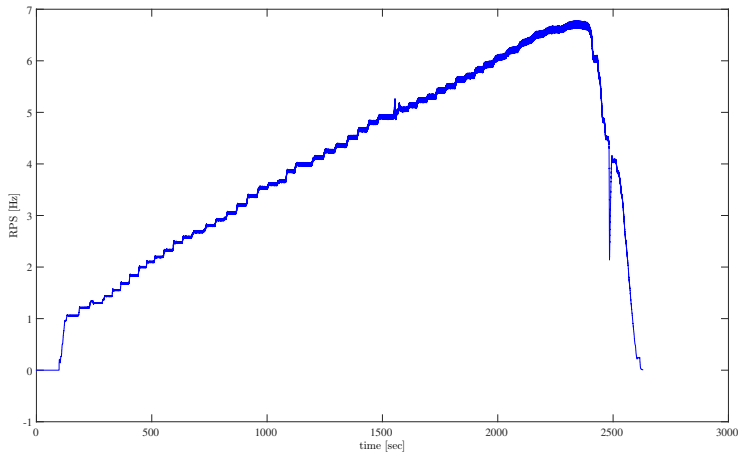

Figure 9: Tachometer signal for the step sweep of the Middle weight setup, showing the constant-frequency plateaus.

Time windows were manually selected for a series of frequency plateaus for each weight setup. The start and end points of these windows were selected such that, based on visual inspection of the signals, no transients were included (resulting from a shift in excitation frequency). Each signal within these time windows (each frequency plateau) was low-pass filtered using a cut-off frequency of 1.5 times the considered excitation frequency. The location of this cut-off frequency was verified to have negligible influence on the amplitudes at the frequency of interest. After removing the zero-frequency component, all the maxima (peaks) within the window were selected for each of the considered sensors: strain gauges 2A,2C - 7A,7C and the 3 accelerometers, see Figure 6. The mean of the selected maxima was taken as the steady-state amplitude of the signal. We used the mean of the amplitudes of strain gauges A and C as the strain amplitude for the associated height on the pile. Henceforth, these measured strain amplitudes will be indicated with ϵ_i with $i = 2, .., 7$. Figure 10 shows an example of the filtered strain gauge responses of the 2.68 Hz frequency plateau (Middle weight setup). The selected maxima are encircled and the steady-state (mean) amplitudes are indicated with the horizontal red lines. The lowest panel of Figure 10,

containing the lowest strain gauge (no. 2) response, shows a less steady signal. The low strain amplitudes occurring at this level in the pile, being excited with a small force amplitude (25.19 kN), are close to the resolution of the strain gauges ($0.1\mu\epsilon$) and the noise contamination is relatively large. We thus have to be aware of less reliable recordings for low forcing levels and locations along the pile where limited bending moments occur.

The corresponding responses of the accelerometers are shown in Figure B.1 in Appendix B. The signals of the accelerometers on the pile (accelerometer 1 and 2, located 1.07 m below the accelerometer on the shaker) were projected onto the direction of the shaker excitation. The amplitudes of this single signal will henceforth be called A_p and those recorded by accelerometer 3 installed on the shaker A_{sh}.

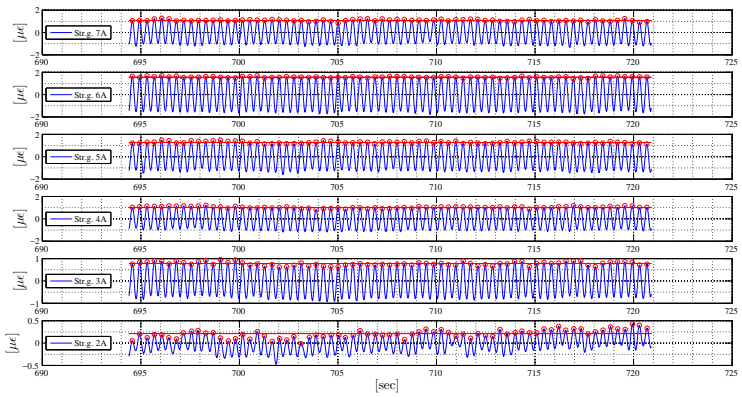

Figure 10: Strain gauge responses after low-pass filtering for frequency plateau 2.68 Hz, Middle weight setup. The red circles indicate the picked peaks, of which the mean was taken over the selected window (red line).

5. Model-based identification

An assessment of the stiffness, damping and possible inertia properties of the observed SSI is given in this section (5.1), in which we focus on the performance of $k_{eff}(z)$ which we derived in Section 3 with the effective stiffness method

[30]. In Section 5.2 we further discuss these identification results and possible implications, and additionally check the performance of the p-y stiffness profile.

5.1. Effective stiffness validation

For the selected (excitation) frequency plateaus of the three weight setups, the measured strain and acceleration amplitudes are compared to those modeled using $k_{eff}(z)$, Figure 4, for a beam on Winkler foundation model. The effective stiffness method [30] yielding $k_{eff}(z)$, will be evaluated/validated by assessing the mismatch between modelled and measured pile response by calculating a single correction factor γ to $k_{eff}(z)$ that minimizes this mismatch. The results of the analyses lead us to consider three 1D models to be used for this minimization, which will be presented in the next subsections: first, a Timoshenko beam on Winkler foundation, which we will call the basic model (Section 5.1.1). Second, this basic model is extended to include a soil-mass resonance effect in which the soil has its own degree of freedom (Section 5.1.2). In Section 5.1.3, instead of the soil acting as a separate resonator, the inertia of the soil is accounted for by means of an added pile mass.

5.1.1. Basic 1D model

A graphical representation of the basic Timoshenko beam on Winkler model used for the stiffness optimization is given in Figure 11.

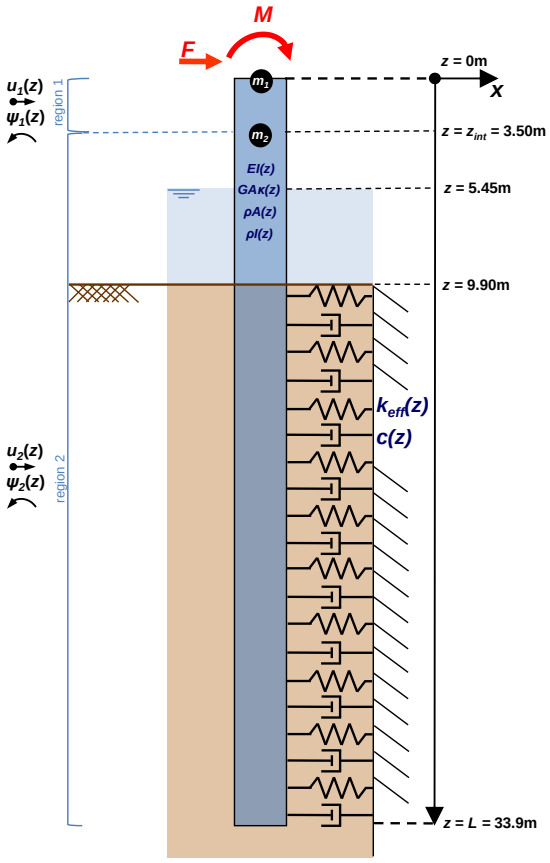

Figure 11: Graphical representation of the basic 1D model, the used reference frame and sign conventions. The symbols are defined in the main text.

In Figure 11, $u(z)$ and $\psi(z)$ are the frequency domain displacements and rotations of the pile respectively. m_2 represents the mass of the internal air-tight platform (5000 kg). Due to the presence of this concentrated mass at 3.5 m below the top of the pile, the model domain is split into 2 regions at which the displacements and rotations (and their derivatives) are solved for. The subscripts "1" and "2" for the displacements and rotations indicate these regions. The concentrated mass m_1 in the model represents the local masses of the MP top flange (4508 kg) and that of the shaker (4500 kg). The trunnions (1800 kg) lie in between these 2 locations; therefore, their mass is partly assigned to

m_1 and partly to m_2. Furthermore, F is the horizontal excitation force amplitude induced by the shaker, M is the overturning moment amplitude caused by the presence of a small vertical lever arm (of on average 0.48 m) between the mid-point of the eccentric masses of the shaker and the MP flange. $k_{eff}(z)$ is the 1D effective Winkler stiffness and $c(z)$ an effective viscous soil damping that covers the sum of the occurring soil damping mechanisms. It is assumed that the shape of the damping dashpots $c(z)$ is related to the shape of the SSI stiffness profile $k_{eff}(z)$ and will be tuned as

$$c(z) = \alpha k_{eff}(z), \tag{2}$$

with α having unit [s] in case of viscous damping (as assumed here). Note that we assume that all damping in the system originates from the interaction with the soil. This is expected to be an acceptable assumption given the expected relatively small damping contributions from the hydrodynamic interaction and the steel hysteresis.

$EI(z)$ is the product of the Young's modulus of the structural steel E and the second moment of area of the cross section of the pile $I(z)$. Due to the fact that the properties of the pile are not constant over the length of the pile, the modelled pile parameters are also made z-dependent. $GA\kappa(z)$ is the product of the shear modulus of the structural steel G, the area of the cross section $A(z)$ and κ, the cross section-dependent Timoshenko shearing coefficient. For the shape of the cylindrical cross section of the pile, $\kappa = 0.53$ was assumed. $\rho A(z)$ is the product of the mass density $\rho(z)$ and $A(z)$. Apart from the steel mass, a soil plug with a density of 1500 kg/m^3 (as was assumed in design) was added to the mass density of the embedded part of the pile. The top 2.75 m of the soil plug was removed and replaced by water, as in reality this soil was excavated from the inner part of the MP to access the embedded electricity cables (see the cable hole in Figure 6). Additionally, in another study [35] it was pointed out that for a stand-alone MP, the quantification of the added mass of the water can have a noticeable effect on the first natural frequency. Therefore, the proposed

frequency- and deflection-shape dependent added mass was taken into account. Besides the properties named here, additional model properties are included in Table B.1 in Appendix B.

If we assume that steady-state conditions apply for the selected amplitudes (Section 4), and that the horizontal harmonic excitation force $\bar{F}$ (time domain) can be approximated by $\bar{F} = F\mathrm{e}^{\mathrm{i}\omega t}$, the equations of motion of the Timoshenko beam model can be expressed in the frequency domain as [36]:

$$GA\kappa\left(\frac{d^2u}{dz^2} - \frac{d\psi}{dz}\right) - K(z)u \quad = 0, \tag{3}$$

$$GA\kappa\left(\frac{du}{dz} - \psi\right) + EI\frac{d^2\psi}{dz^2} + \omega^2\rho I\psi \quad = 0, \tag{4}$$

with the dynamic stiffness $K(z)$ equal to

$$K(z) = k_{eff}(z) + \mathrm{i}\omega c(z) - \omega^2\rho A. \tag{5}$$

Note that for brevity we omit the z-dependence of the structural properties. Additionally, due to the minor and localized z-dependence of the wall thickness and for the considered range of frequencies, we verified that constant pile properties in the second order terms given above can be assumed.

The considered boundary conditions are:

$$GA\kappa\left(\frac{du_1}{dz} - \psi_1\right)\Big|_{z=0} \quad = -F - \omega^2 m_1 u(0), \tag{6}$$

$$EI\frac{d\psi_1}{dz}\Big|_{z=0} \quad = M, \tag{7}$$

$$GA\kappa\left(\frac{du_2}{dz} - \psi_2\right)\Big|_{z=L} \quad = 0, \tag{8}$$

$$EI\frac{d\psi_2}{dz}\Big|_{z=L} \quad = 0. \tag{9}$$

The presence of m_2 at $z = z_{int} = 3.5$ m (Figure 11) can be taken into account

by formulating the interface conditions:

$$u_1(z_{int}) - u_2(z_{int}) = 0, \tag{10}$$

$$\tfrac{du_1}{dz}\big|_{z_{int}} - \tfrac{du_2}{dz}\big|_{z_{int}} = 0, \tag{11}$$

$$GA\kappa\Big((\tfrac{du_1}{dz} - \psi_1) - (\tfrac{du_2}{dz} - \psi_2)\Big)\Big|_{z_{int}} = \omega^2 m_2 u_1(z_{int}), \tag{12}$$

$$\tfrac{d\psi_1}{dz}\big|_{z_{int}} - \tfrac{d\psi_2}{dz}\big|_{z_{int}} = 0. \tag{13}$$

The above relations ensure (from top to bottom) the continuity of displacement and slope, a dynamic shear force balance, and continuity of bending moment at the interface location.

For the excitation of the model we can apply the force of the shaker (equation 6). Alternatively, we can use the acceleration amplitude that was measured by the accelerometer attached to the shaker. In that case, the boundary condition given by equation 6 is replaced by

$$u_1(0) = \frac{A_{sh}}{\omega^2}, \tag{14}$$

in which A_{sh} is the steady-state acceleration amplitude measured on the shaker. In calculating the modeled response by either using equation 6 (force-controlled) or 14 (acceleration-controlled) as a boundary condition, a mismatch was observed between these two modeled responses. If we presume that measurement errors can be neglected, this mismatch could be caused by the fact that the model does not fully reflect the correct physics of the system. In the following analyses, both cases (force- and acceleration-controlled) were considered to determine what stiffness correction factor is needed for the modeled response to match the measurements.

Stiffness optimization

To reduce the mismatch with the measurements, the stiffness profile of the 1D model was optimized by applying a single factor, γ, to the 1D effective stiffness profile $k_{_{eff}}(z)$. In this, we thus assume the shape of the previously derived

effective 1D stiffness to be correct, but we search for a (single) correction factor γ so that the predicted response globally matches the measured one for each of the selected frequencies; we assign equal weight to the fit of all 6 strain gauge positions and the 2 accelerometers. The stiffness correction factor γ is defined as the factor applied to the effective stiffness $k_{_{eff}}(z)$ (Figure 4) that minimizes the global root mean square error (L_2 norm):

$$\min_{\gamma} \left| \left(\frac{\sum_{i=2}^{i=7} |\epsilon_i - \overline{\epsilon}_{i(\gamma)}|^2}{\sum_{i=2}^{i=7} |\epsilon_i|^2} + \frac{|A_{sh} - \overline{A}_{sh(\gamma)}|^2}{|A_{sh}|^2} + \frac{|A_p - \overline{A}_{p(\gamma)}|^2}{|A_p|^2} \right)^{\frac{1}{2}} \right|. \tag{15}$$

The overlined symbols in Equation 15 indicate that these are the corresponding modeled quantities. The modeled strain is computed as

$$\overline{\epsilon}_i = \frac{D}{2} \left| \frac{d\psi}{dz} \Big|_{z_i} \right|, \tag{16}$$

with D the diameter of the pile.

Resulting frequency-dependent stiffness

The resulting stiffness correction factors γ for the three setups are given in Figure 12, in which the dotted lines are the factors obtained with a force-controlled model (Equation 6) and the continuous lines are those obtained when using an acceleration-controlled model (Equation 14). The green line reflects the aim; a factor γ of 1 indicates a spot on match.

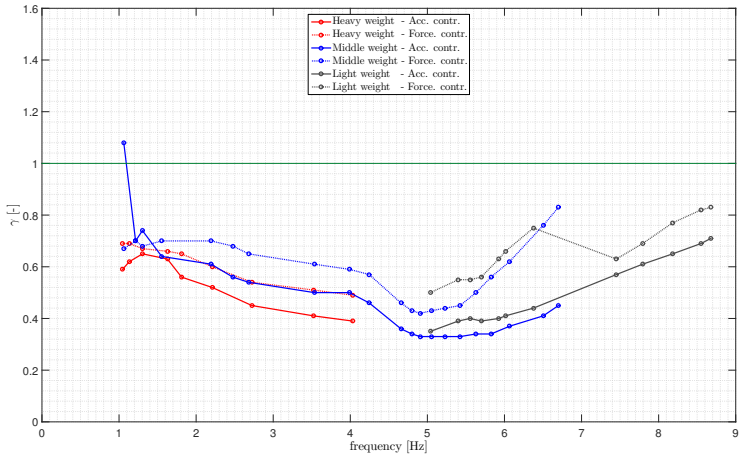

Figure 12: Correction factors γ applied to the effective 1D stiffness profile (as presented in Figure 4) to minimize the mismatch between modeled and measured response amplitudes of the 3 weight setups. The continuous lines represent the factors found with an acceleration-controlled model, and the dotted lines are the factors found with a force-controlled model. The green line reflects the aim; a factor γ of 1 indicates a spot on match of the measured and the (unadjusted) modelled response.

In Figure 12 the following trends can be observed. First, the stiffness slightly decreases with frequency and reaches a minimum situated between 4.5 and 5.5 Hz, after which it increases again. The stiffness thus seems frequency dependent; $\gamma = \gamma(f)$. Second, a force or displacement dependency of the stiffness can be observed: from the more or less parallel lines of the Heavy and Middle weight setup (higher stiffness for a lighter weight/smaller force), but also from the parallel lines of the Middle and Light weight setup. As a reference, the force ratios of the setups for an equal excitation frequency are listed in Table 1. Finally, the first point for the Middle weight setup is an outlier, and should therefore not be considered in defining a trend.

It could be reasoned that the actual stiffness is somewhere in between the two factors given in Figure 12 (force- and acceleration-controlled models). Figure 13 gives an example fit of the force-controlled and acceleration-controlled modelled strains with respect to the measured strains of the Heavy weight setup,

with excitation at 1.045 Hz, for a mean γ of 0.64 applied to the original effective 1D stiffness profile. For extra insight, also the modelled shear forces and displacements are shown.

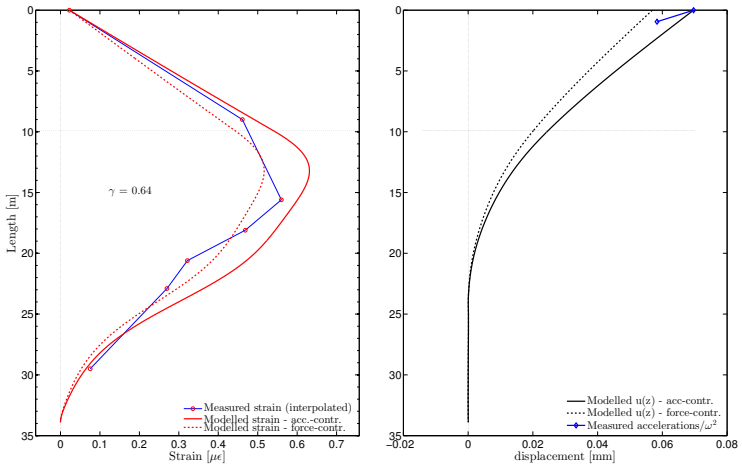

Figure 13: Match in strains with a stiffness correction factor γ equal to the mean of the force- and acceleration-controlled factors from Figure 12, for the Heavy weight setup, excitation frequency of 1.045 Hz. The absolute values of both the acceleration- and force-controlled modelled responses are shown in terms of shear force and strain (left panel) and displacements (right panel). The vertical axis is the length of the pile, where the mudline is indicated at 9.9 m.

To overcome the discrepancy between the force- and acceleration-controlled responses, we consider internal transfers of the system, sometimes also referred to as (internal) transmissibility: the ratio between the strain amplitudes at several locations and the displacement amplitudes, u_p, retrieved from the accelerometer attached to the top of the pile ($u_p = \frac{A_p}{\omega^2}$, assuming no drift in the displacements or velocities (integration constants equal to zero)). The advantage of considering this quantity is that it is (excitation) source independent. In optimizing the stiffness of the 1D model to match the transmissibilities of the measurements, the following minimization function is used:

$$\min_{\gamma} \left| \left(\frac{\sum_{i=2}^{i=7} |T_i - \overline{T}_{(\gamma)i}|^2}{\sum_{i=2}^{i=7} |T_i|^2} \right)^{\frac{1}{2}} \right|, \tag{17}$$

with the (amplitude of the) internal transmissibility function given as

$$T_i(f) = \frac{\epsilon_i(f)}{u_p(f)} = \frac{\epsilon_i(f)\omega^2}{A_p(f)}. \tag{18}$$

The resulting stiffness correction factors γ are given by the thick lines in Figure 14. As a reference, the $\gamma's$ of Figure 12 are also included with thin lines. The acceleration-controlled model was used to calculate the transmissibilities, but the force-controlled model led to nearly the same correction factor γ - indicating the desired source independency. Therefore, henceforth only the transmissibilities will be considered for further stiffness optimization.

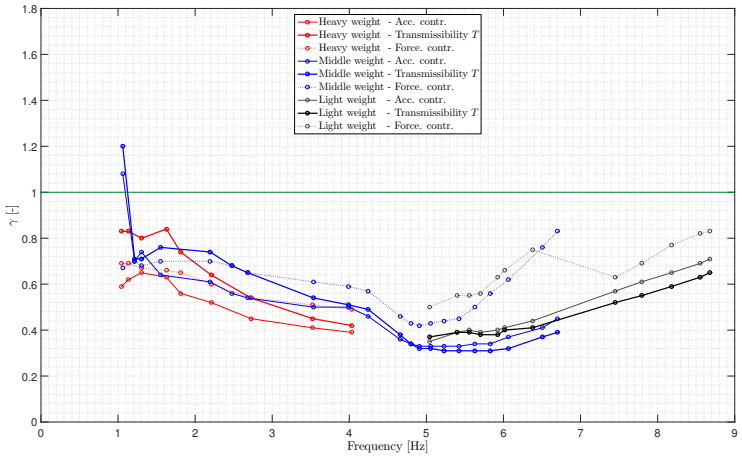

Figure 14: Factors γ applied to the effective 1D stiffness profile (as presented in Section 3) to minimize the mismatch between modeled and measured transmissibilities T (Equation 17) of the 3 weight setups (thick continuous lines). As a reference, the factors retrieved for direct minimization of strain and acceleration error (Equation 15) with the acceleration-controlled (thin continuous lines) and force-controlled models (thin dotted lines) are shown.

Figure 15 shows the internal transfers (Equation 18) corresponding to the frequency-dependent stiffness γ of the Middle weight setup (thick blue continuous line in Figure 14). We will restrict this paper to considering transfer functions and transmissibilities retrieved for the Middle weight setup only, as the tested frequency range for this setup is broadest.

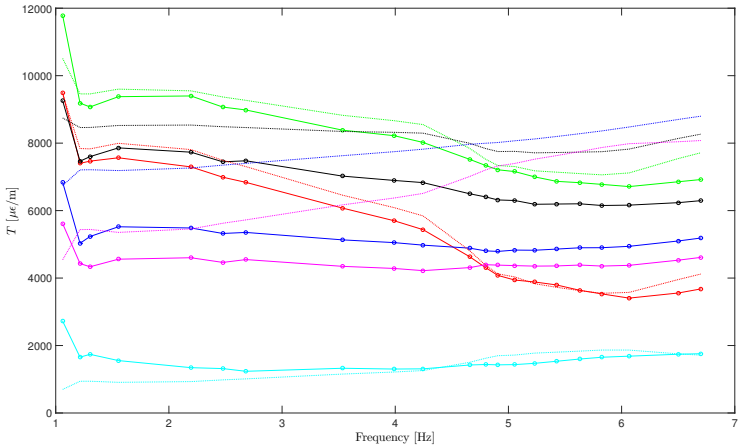

Figure 15: Measured (continuous lines) and modeled (dotted lines) transmissibility functions (Equation 18) of the strain gauges for the Middle weight setup, using factors on stiffness γ given by the thick blue line given in Figure 14: optimization for transmissibility.

As we do not vary the shape of the stiffness profile retrieved from the 3D model, there is no good match for all individual sensor locations and for all frequencies in Figure 15. Still, the internal transfers of the two strain gauges located closest to the top (where the largest strains occur; red and green lines in Figure 15) match reasonably well for the entire frequency range.

To assess the resonance of the system and estimate the effective damping, we can compute (the amplitude of) the transfer functions by dividing the responses by the input force (Equation 1):

$$H_i(f) = \frac{\epsilon_i(f)}{F(f)}. \tag{19}$$

When using the stiffness reduction factors as given by the thick blue continuous line in Figure 14 (optimization for transmissibility for the Middle weight setup), we get (force-controlled) modelled transfer functions given in Figure 16; the corresponding measured transfer functions are included for comparison.

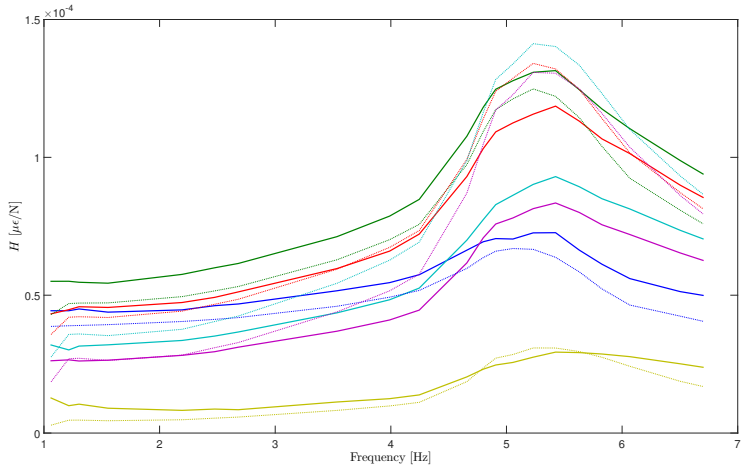

Figure 16: Measured (continuous lines) and modeled (dotted lines) transfer functions for the strain gauges along the pile (Middle weight setup). For the modeled response, the factors on stiffness as given by the thick blue line given in Figure 14 (optimization for transmissibilities: Equation 17) were applied to the effective 1D soil stiffness profile given in Figure 4. The dashpot coefficients were tuned to a value of $c(z) = 2.08 \cdot 10^{-2} k_{eff}(z)$, yielding a critical damping ratio of 20%.

In Figure 16 we observe a resonance frequency around 5.4 Hz. In addition, the figure shows that the dotted lines of the modelled response do not completely match the measured (continuous lines) for all strain gauges, but rather correspond in a global way (as discussed previously). Furthermore, we see that the modeled strain transfer functions for numbers 3-6 draw closer towards each other at resonance and post-resonance than those that were measured. This is related to a localized smaller dynamic stiffness (Equation 5) in the modelled response at these frequencies; either the modelled inertia contribution or the modelled frequency-dependent stiffness is not fully correct. This can also be clearly seen in fits for higher frequencies shown in Figures B.3 and B.4 in Appendix B; the modelled response shows larger inertia effect (or smaller stiffness) than measured for depths larger than 17 m. Finally, the modeled dynamic stiffness (Equation 5) for the post-resonance regime seems to be a bit larger than measured, indicating either too small mass $\rho A(z)$ or too large stiffness.

Damping estimation

The resonance peak allows us to tune the dashpot coefficients $c(z)$ for the modeled response. In actual fact, finding the matching stiffness and damping is done in 1 or 2 iterations: with the updated dashpot coefficients, the stiffness correction factors are re-assessed, etc. For the modeled transfer functions in Figure 16, $\alpha = 2.08 \cdot 10^{-2}$s (Equation 2). Using the obtained damping coefficients and a mean stiffness correction factor γ of the frequencies around resonance to simulate a response, we extracted the damping contribution of the soil with the half-power bandwidth method [37], yielding a critical damping ratio of $\zeta = 20\%$ for this stand-alone MP. Note that the dashpots coefficients are tuned based on a visual fit of the transfer functions. The stated damping ratio should therefore be considered an estimate. An analysis of the variance of this number is beyond the scope of this paper. In Section 5.2.4 we discuss how this damping contribution could relate to the damping of the full OWT structure.

Concluding this subsection, we may state that a frequency-dependent stiffness is needed to match the measurements with the response predicted by a beam on Winkler foundation model as shown in Figure 11. Three frequency regimes can be distinguished: a pre-resonance regime (up to 4.2 Hz) in which the stiffness slightly decreases with frequency, a resonance regime (4.2 - 6 Hz) in which the stiffness decreases further, and a post-resonance regime where the stiffness sharply increases (Figure 14). Although we lack measurements below 1 Hz, it is expected that the effective 1D stiffness as presented in Figure 4 over-estimates the true stiffness at low frequencies with about 22% ($\gamma = 0.78$), see low frequency $\gamma(f)$ in Figure 14. Optimizing the stiffness to match the measured internal transmissibilities seems a good approach to overcome the ambiguity in choosing the correct excitation boundary condition in the model. From the transfer functions, the effective damping ratio of the system was estimated to be 20% of critical - assumed to be mainly caused by the interaction with the soil. In the next sections we investigate whether the observed frequency depen-

dency of the stiffness of the system can be attributed purely to the effective soil stiffness (as was assumed in this section), or whether other mechanisms might be responsible for the measured response.

5.1.2. Soil resonator model

The resonance peak observed in Figure 16 and the associated decrease in stiffness around these frequencies (Figure 14) can be related to the first resonance frequency of the monopile-soil system. However, it might also be related to a resonance of the soil itself; i.e., a resonance of the layered system or a resonance as commonly observed in cavity expansion problems [38]. If this is the case, the soil acts as a resonator, highly influencing the total system response at the resonance and post-resonance frequencies. To assess this possibility, a distributed resonator mass $M_s(z)$ is added to the 1D model, as shown in Figure 17.

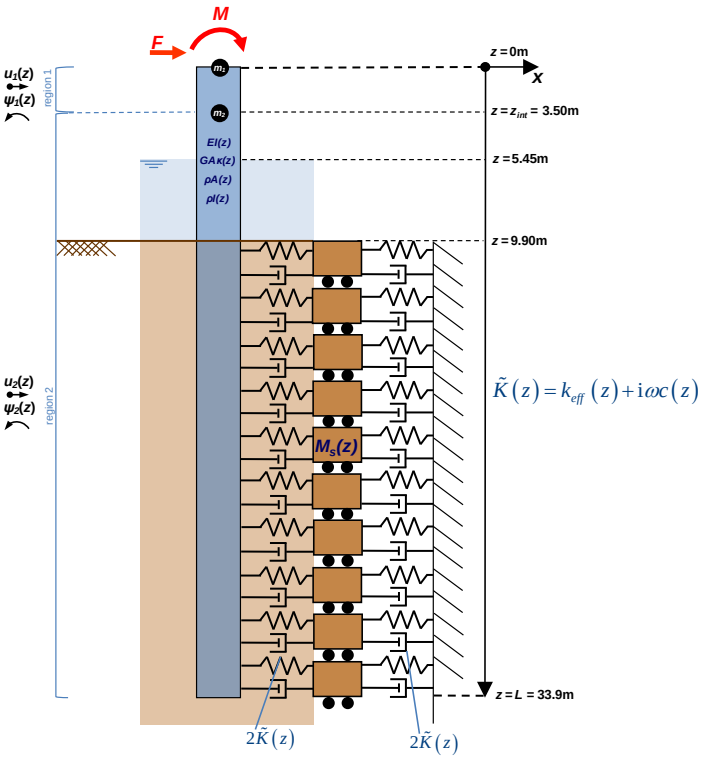

Figure 17: The 1D model including a distributed resonator.

The addition of this mass to the 1D model only modifies the soil-resistance term in Equation 3 and the expression for the dynamic stiffness (Equation 5), while the rest of the governing equations (4, 6 - 13) remain unchanged. Equation 3 becomes:

$$GA\kappa\Big(\frac{d^2u}{dz^2} - \frac{d\psi}{dz}\Big) - \Big(2\widetilde{K}(z)\frac{(2\widetilde{K}(z) - M_s(z)\omega^2)}{(4\widetilde{K}(z) - M_s(z)\omega^2)} - \omega^2\rho A\Big)u = 0, \tag{20}$$

with

$$\widetilde{K}(z) = k_{eff}(z) + \mathrm{i}\omega c(z), \tag{21}$$

and

$$M_s(z) = \frac{2k_{eff}(z)}{(2\pi f_s)^2}, \tag{22}$$

with f_s the resonance frequency of the soil. In the case the soil acts as a resonator, the effective soil stiffness $k_{eff}(z)$ can be assumed to be frequency-

independent; the decrease in resistance with frequency observed in Figure 14 is then attributed to the dynamic interaction with the soil mass $M_s(z)$. This frequency-independent stiffness can be identified using the optimization results for the lower frequencies (note that, for low frequencies, the soil resistance term in Equation 20 equals that of the basic model (Equation 3)). Neglecting the outlier of the lowest frequency of the Middle weight setup in Figure 14 (blue line), taking an average constant γ of 0.78 for the lower frequencies seems reasonable. In matching the transfer functions by tuning the resonator frequency f_s (therefore the magnitude of the soil mass M_s, Equation 22) and the damping $c(z)$, we however noticed that the shape of the resonance peak was not well captured when assuming frequency independent stiffness. We therefore performed a stiffness optimization of which the resulting $\gamma(f)$ are presented in Figure 18. This $\gamma(f)$ was determined with $f_s = 6.7$ Hz and a damping tuning coefficient $\alpha = 7.9 \cdot 10^{-3}$ - based on the initial fit of the transfer functions.

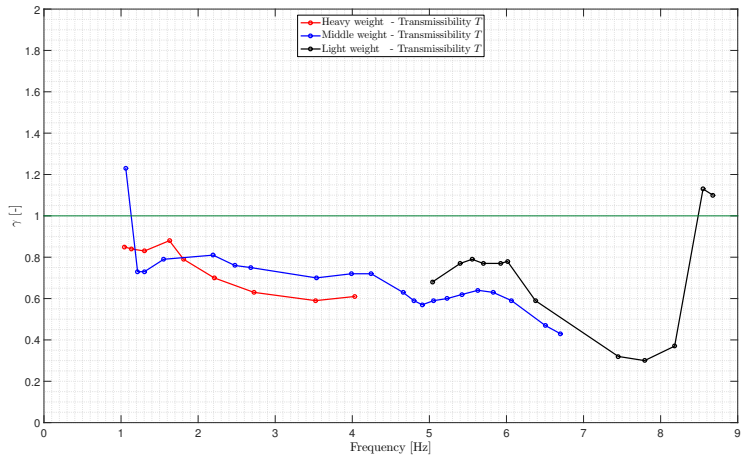

Figure 18: Stiffness correction factors γ found for optimizing a mass-resonator model with $f_s = 6.7$ Hz (Equation 22) and $\alpha = 7.9 \cdot 10^{-3}$, to match the measured internal transmissibility function $T_i(f)$ (Equation 18).

In Figure 18 we indeed observe - due to the presence of the resonator - a more constant stiffness ($\gamma(f)$) for the pre-resonance and resonance regime, a drop in stiffness in the post-resonance regime, and eventually a similar stiffening as

observed in Figure 14 for the highest frequencies. Using this $\gamma(f)$, we further tuned the soil resonator frequency to $f_s = 6.95$ Hz and damping tuning coefficient $\alpha = 9.6 \cdot 10^{-3}$ to yield the transmissibility and transfer functions as presented in Figures 19 and 20. Applying the same damping determination method as described in previous Section 5.1.1, these dashpot coefficients yield a critical damping ratio of $\zeta = 12.6\%$. Note however, that the presence of the resonator causes the main resonance peak to have a less symmetric shape, making the half-power bandwidth method only an approximate method to determine the damping of this system.

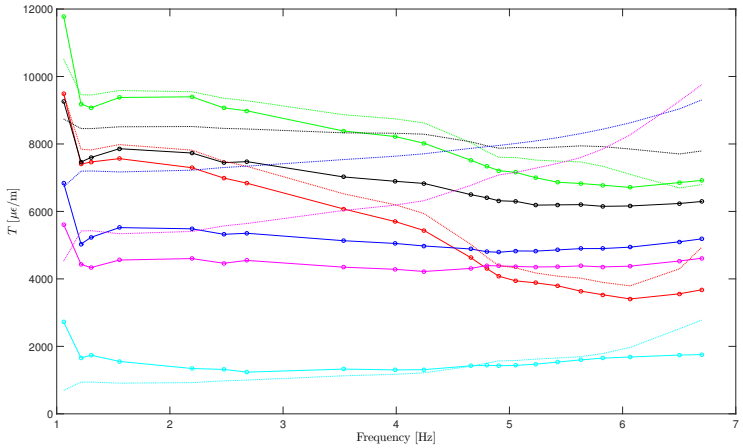

Figure 19: Measured (continuous lines) and modeled (dotted lines) transmissibility functions (Equation 18) of the strain gauges for the Middle weight setup. The modeled response is calculated with the mass-resonator model of Figure 17 with a frequency-dependent stiffness correction factors $\gamma(f)$ (blue line, Figure 18) applied to the effective 1D soil stiffness profile. Furthermore, $\alpha = 9.6 \cdot 10^{-3}$, and $f_s = 6.95$ Hz.

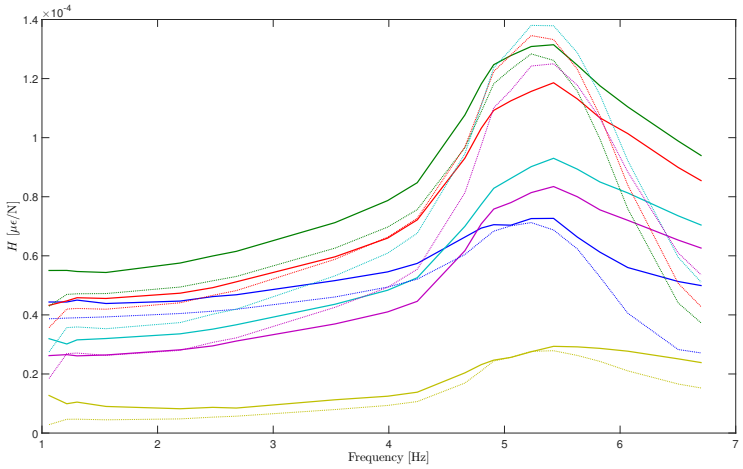

Figure 20: Measured (continuous lines) and modeled (dotted lines) transfer functions for the strain gauges along the pile (Middle weight setup). The modeled response is calculated with the mass-resonator model of Figure 17 with frequency-dependent stiffness correction factors $\gamma(f)$ (blue line, Figure 18) applied to the effective 1D stiffness profile. The dashpot coefficients were tuned to $\alpha = 9.6 \cdot 10^{-3}$, yielding a critical damping ratio of 12.6%. The resonance frequency of the soil was tuned to $f_s = 6.95$ Hz.

The resulting matches of this soil-mass resonator model with the measurements in terms of transmissibilities and transfer functions are acceptable, however, those of the basic model seem better (Figures 15 and 16). Especially the match of the transfer functions for the post-resonance regime is better using the basic model; in case of the resonator model, the dynamic stiffness seems too large for these frequencies. Additionally, the transmissibility functions seem to match better using the basic model.

5.1.3. Added mass model

In the case the observed decrease in dynamic stiffness (Equation 5) with frequency is indeed caused by extra mobilized inertia, this can also be due to a more direct added mass of the soil in the vicinity of the pile (as opposed to the previous analyzed soil resonator system). This is incorporated in the basic model (Figure 11) by multiplying the embedded part of the distributed mass

$\rho A(z)$ by a factor η.

Also in this case it was observed that a constant stiffness with frequency (again a γ of 0.78) does not adequately capture the post-resonance regime. Performing an iteration for $\gamma(f)$, η and $c(z)$ (based on transfer functions and stiffness optimization, Equation 17), yields the final $\gamma(f)$, transmissibility and transfer functions as shown in Figures 21, 22 and 23, respectively. The soil added mass factor is in this case $\eta = 3.4$ (of the original embedded pile mass) and dashpot tuning coefficient $\alpha = 8.4 \cdot 10^{-3}$, yielding a damping ratio $\zeta = 11\%$ critical for the MP-only system.

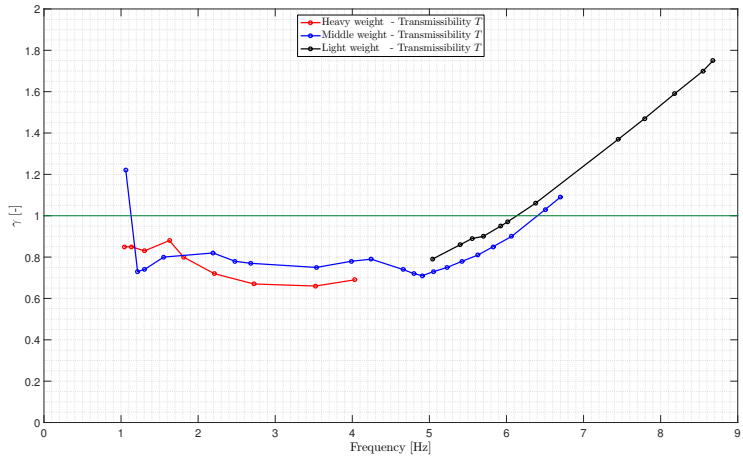

Figure 21: Stiffness correction factors γ found for optimizing the basic model with an added mass factor $\eta = 3.4$ times the embedded pile mass, and $\alpha = 8.4 \cdot 10^{-3}$, to match the measured internal transmissibility function T.

In Figure 21 we see - as expected - a more constant, frequency-independent stiffness (as opposed to those found with the basic model) up until the post-resonance regime, after which again a sharp increase in stiffness factors is observed.

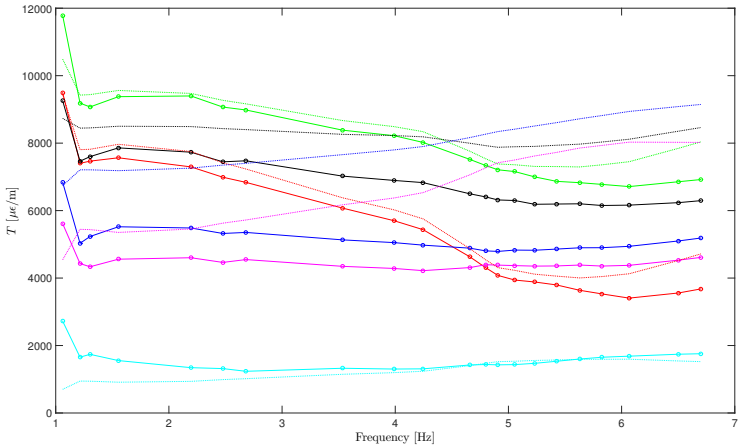

Figure 22: Measured (continuous lines) and modeled (dotted lines) transmissibility functions (Equation 18) of the strain gauges for the Middle weight setup. The modeled response is calculated with the basic model including added mass of the soil, with a frequency dependent stiffness correction factor γ (blue line, Figure 21) applied to the effective 1D soil stiffness profile. Furthermore, $c(z) = 8.4 \cdot 10^{-3} k_{eff}(z)$, and an added mass factor $\eta = 3.4$ times the original embedded pile mass.

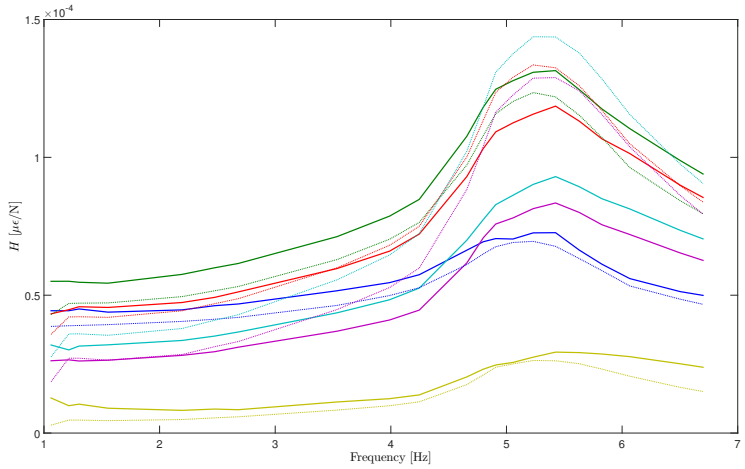

Figure 23: Measured (continuous lines) and modeled (dotted lines) transfer functions for the strain gauges along the pile (Middle weight setup). The modeled response is calculated with the basic model of Figure 11 including added (soil) mass for the embedded part of the pile ($\eta = 3.4$), and the frequency-dependent factors on stiffness γ (applied to the effective 1D stiffness) given by the blue line in Figure 21. The dashpot coefficients were tuned to $\alpha = 8.4 \cdot 10^{-3}$, yielding a critical damping ratio of 11%.

The transmissibility functions and transfer functions are reasonably matched. However, also this model does not seem to perform better in matching the modelled and measured functions than the basic model (Figures 15 and 16). Nevertheless, the match in transfer functions for the post-resonance frequencies is better than that of the soil-mass resonator model (Figure 19). Concluding, the two models incorporating more mobilized soil mass seem to allow for a frequency-independent stiffness for the pre-resonance regime (up to 4 Hz), however do not permit to exclude a frequency dependency of the stiffness for the resonance and post-resonance regimes.

5.2. Discussion

In this section we discuss the 3 observed frequency regimes: the low, pre-resonance regime relevant for OWTs, the resonance, and the post-resonance regime. We compare how the design p-y curve stiffness performs in predicting

the measurement data, and how the presented findings relate to the preliminary identified full OWT structure natural frequency. Additionally, the full structure damping and possible soil non-linearity are discussed.

5.2.1. Low frequency stiffness validation - relevant for OWT design: effective 1D method vs p-y method

Independent of the assumptions regarding the soil (added) mass, all 3 stiffness optimization results indicate that the effective 1D stiffness over-estimates the occurring stiffness at low frequencies with roughly 20% (γ = 0.78 - 0.8). Although we do not have measurements for frequencies lower than 1Hz, it is reasonable to assume the stiffness between 0 and 1 Hz to be either higher or equal to that observed at 1-2 Hz. A correction factor of 0.8 is not insignificant, however, given the uncertainty related in dynamic soil characterization and SSI modelling, the 1D effective stiffness method [30] is deemed promising. Furthermore, it is expected that the method can be improved; a fully linear elastic model was used in which the soil elements were attached to the shell elements of the pile. Nonlinearities such as sliding between soil and pile and installation effects which cause a weaker interface region of the soil around the pile, can be incorporated in the future. Additionally, the fit of the 1D and 3D results can also be improved; the right panel of Figure 5 shows that the 3D strains are somewhat higher with a maximum at a lower location than that of the 1D model, so in actual fact, the 1D effective model behaves more stiff than the 3D model. Finally, another aspect that can bring the measured and predicted stiffness closer together is the pile set-up effect; although there is still much uncertainty in this research field [39], the capacity (and SSI stiffness) of piles in both clay and sand is known to increase with time [40]. The here presented tests were performed 50 days after the installation of the pile, and the "aging" process is known to have time frames larger than 400 days [41].

In judging the performance of the proposed stiffness method [30] it is also rele-

vant to see what strain levels the design standard predicts. As expected, the *p-y* curve method proved to significantly underestimate the stiffness experienced by the pile. We therefore also computed the stiffness correction factors γ needed to be applied to the *p-y* initial stiffness to match the measured pile responses. For this exercise, we took a best estimate set of *p-y* curves; minimum conservatism with respect to the input parameters and half a meter of scour was assumed. For the low frequencies, a γ of roughly 2.4 was needed to best match the internal transmissibilities. The more conservative design *p-y* curves yielded a γ of around 5. The $\gamma(f)$ for the best estimate *p-y* initial stiffness is shown in Figure 24. For the *p-y* stiffness, the low-frequency limit of γ is less clear due to the large spread in stiffness factors for the low-frequency regime. It is expected that this is caused by the fact that this *p-y* profile is less stiff than the effective 1D stiffness, and also the profile shape might be erroneous.

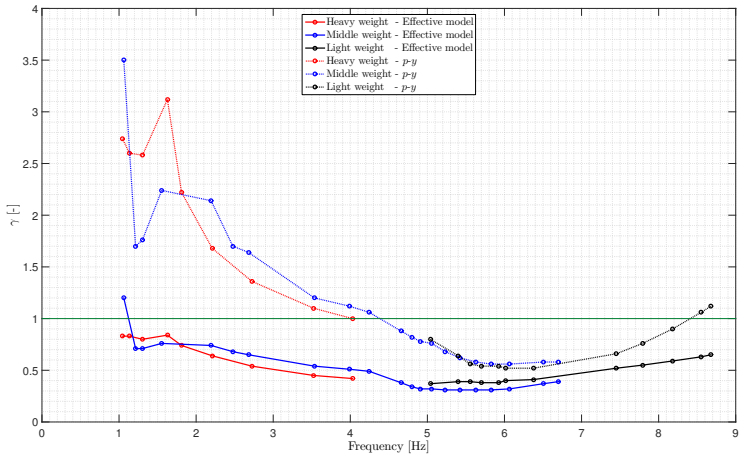

Figure 24: Stiffness correction factors γ found for optimizing the basic model (Figure 11) with the *p-y* initial stiffness profile (Figure 4), to match the measured internal transmissibility function T. As a reference, the $\gamma(f)$ for the effective stiffness of Figure 14 are also shown.

5.2.2. Resonance frequency

In Sections 5.1.2 and 5.1.3 we examined whether the observed decrease in dynamic stiffness (Equation 5) in the pre-resonance regime could be attributed to

the mobilization of (extra) soil mass. In the case of soil resonance, the observed resonance in the transfer functions can be related to a natural frequency of the soil layer f_s, which can be approximated as

$$f_{s,n} = \frac{(2n-1)C_s}{4H}, \tag{23}$$

where n is the mode number, H the soil layer thickness and C_s the shear-wave velocity. The effective thickness of the layer in this respect is debatable, but often the depth until the location of bedrock is taken. For a first resonance frequency of 5.42 Hz as observed in the transfer functions of the Middle weight setup, and an approximate shear-wave velocity of $C_s \approx 300$ m/s (see Figure A.2), the bedrock would be located at about 14 m depth, which we know is not the case. At this part of the Netherlands, bedrock known as the Appelscha formation is present at 60-100 m depth. Assuming the same C_s, the first mode resonance frequency of the soil would be located at 1.25 Hz ($H = 60$ m) or 0.75 Hz ($H = 100$ m). If the observed resonance frequency is indeed associated with the soil, it is more likely to belong to the second soil mode, and in that case the presence of the first mode is, apparently, not observable in our data. Altogether, it is hard to draw solid conclusions about the dynamics (in terms of (added) mass, stiffness and resonance frequencies) of this layered soil system without knowledge about the position of the bedrock and the use of a dynamic continuum model of the soil. Despite the simplifications of the 1D model, the low-frequency range stiffness can be extracted (as it is more or less equal for the 3 tested models).

We believe however, that the basic model (possibly including some added mass of the soil) is most applicable, as the transfer functions and transmissibilities are best matched with this model. Also, as will be discussed in Section 5.2.4, the estimated soil damping contribution from this model agrees best with the identified total damping of the idling OWT.

To further assess the performance of the different soil stiffness profiles, we com-

pared the predicted (modelled) fundamental natural frequency f_1 with that identified from preliminary measurements on the operational OWT (full structure). A natural frequency of $f_1 = 0.296$ Hz was identified for the fore-aft bending mode with the turbine in idling state. Four different stiffness profiles were used in an excitation decay simulation (including aerodynamics) using BHawC (the aeroelastic code used by Siemens Wind Power): the effective stiffness profiles $k_{eff}(z)$, the optimized low-frequency profile ($\gamma = 0.78$), the best-estimate p-y stiffness profile and the optimized best-estimate p-y stiffness profile ($\gamma = 2.4$ is estimated to be applicable for the low-frequency limit). The resulting natural frequencies are listed in Table 2.

	f_1 **- idling - [Hz]**	**Δ w.r.t. identified**
Identified	0.296	-
p-y **curve**	0.295	-0.34%
p-y **curve** $\gamma = 2.4$	0.300	+1.35%
Eff. stiffness	0.306	+3.38 %
Eff. stiff. $\gamma = 0.78$	0.305	+3.04 %

Table 2: Overview of the identified and predicted (BHawC-simulated) natural frequencies using various soil stiffness profiles. The frequency belongs to the fore-aft vibrational mode (first bending mode) of the full OWT structure in idling state.

From the frequencies listed in the Table 2, we observe that soil models whose responses match the shaker measurements best, seem to slightly over-predict the fundamental natural frequency of the full OWT. Although we can at this stage only speculate on the reason for this deviation, it could be caused by a structural model error [1], but could also be related to the soil excavation that took place after the shaker measurements; 2 soil wedges of 2.5 m depth, base-width

[1] A in-house study [42] showed that for instance a 2% mass deviation of the nacelle (which is a realistic deviance) can lead to ±0.5% variation of the natural frequency. Of course such a relation is structure and site dependent. Similar sensitivity relations can be found in [1].

of 3 m and slopes of 1:2.5 were excavated at the North and South-East sides of the MP to insert the electric cables. These wedges were subsequently refilled, resulting in weaker soil than during the shaker experiment. As the stiffness of the shallow soil layers highly influences the overall SSI stiffness, the softening of this region leads to a lower natural frequency.

From Table 2 we also observe that the differences in predicting the natural frequencies (the errors) are much smaller than would be expected from the analyses of the pile-only response. This is caused by the smaller influence the soil stiffness has on the full structure (extending 95 m above water level) as opposed to the monopile only (extending 5.45 m above water level). Beneficially for the design community, the error made in modelling the soil reaction, converges to much smaller values for tall OWT stuctures than foundation-only structures. In line with this reasoning, we can state that, due to the high sensitivity of a MP-only structure to the soil-reaction, such a system is much more fit for identifying (validating) a soil model than a full OWT system. Aiming to visualize this sensitivity, Figure 25 shows the relation between the natural frequencies versus variation in the stiffness (for both the p-y and the effective stiffness profiles) for the MP-only case and the full structure case. Similar as in Table 2, the full structure natural frequencies were extracted from excitation decay simulation using BHawC. For equal comparison between the MP-only cases (upper two panels), the bounds of the vertical axes of these figures (the variation of natural frequencies) are set to 33% variation around the central frequency. All four panels show equal stiffness scaling factors in the range of 0.1 to 4 (horizontal axes).

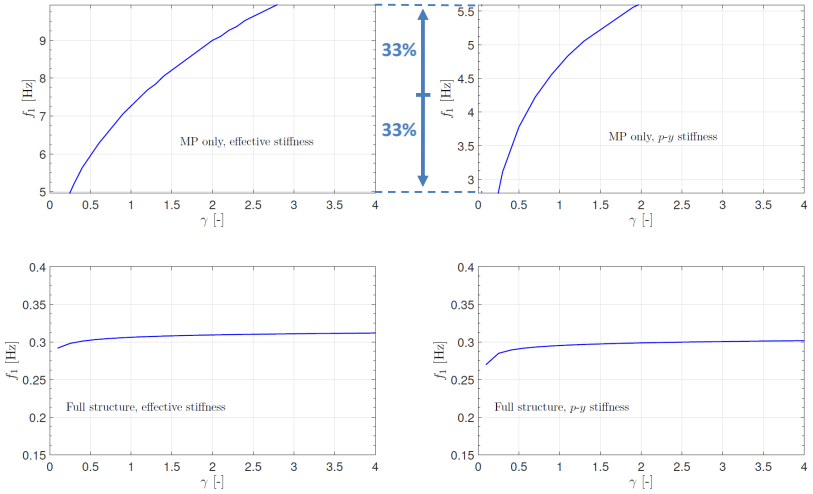

Figure 25: Sensitivity of the natural frequency to the effective and p-y stiffness profiles for the monopile-only case (calculated with the basic model, Figure 11) and the full OWT structure (extracted from excitation decay simulation using BHawC). For equal comparison between the MP-only cases, the bounds of the vertical axes of the upper panels are set to a 33% variation around the central frequency.

Figure 25 also reflects the asymptotic relation between the stiffness and the natural frequency of the full OWT structure; the stiffer the profile, the closer we get to the situation where the pile can be considered as clamped at mudline (a cantilever), the smaller the variation in natural frequency. This trend can be observed by comparing the lower p-y stiffness for the full structure (lower right panel), and the larger effective stiffness which converges even faster (lower left panel). Therefore, the added value of monopile-only testing is larger for stiff site conditions; a softer soil profile is more fit for soil-model validation based on the full OWT response due to a larger sensitivity. This short study has been included to reflect on the fact that soil models are often judged solely on the natural frequencies of the full OWT; due to (other) structural uncertainties and a lower sensitivity towards the soil stiffness for stiff profiles, it is not surprising that the measured frequencies of installed OWTs can deviate a few percentages

(often $< 5\%$ [1]) from the design target[2] - even for 'almost correct' soil models. For similar reasons pile-only measurements can be considered more fit for identifying soil damping than full OWT records. Additionally, pile-only systems lack the aerodynamic damping contributions, making the identification of the soil contribution less ambiguous.

5.2.3. Post-resonance frequency

A stiffness increase occurs at post-resonance frequencies. We observe this in the stiffness optimization of the 3 models, however, most pronounced for the basic model (Figure 14), and the basic model with added mass (Figure 21). Although a preliminary investigation [43] indicated no pore pressure build-up recorded in the piezometers in the soil until 4 Hz (only the Heavy weight setup was analyzed), the undrained behavior of the soil is a physical mechanism that might cause this stiffness increase at the higher frequencies .

5.2.4. Damping of OWT

In Section 5.1.1 we estimated the damping contribution of the soil for the stand-alone MP to yield a damping ratio of $\zeta = 20\%$ (for the basic model, Figure 11). To get a rough idea of this contribution to the damping of the full structure (including tower and RNA), we extended the top of the MP to the hub height and included a point mass at the top representing the RNA. This mass was tuned to match the natural frequency that was identified for the full structure. Furthermore, a γ of 0.78 was applied to the effective stiffness as this seems to be applicable for the low-frequency regime (see Figure 14). Applying the half-power bandwidth method on the response of this simplified full-structure model

[2] A deviation within $\pm 5\%$ is often accepted by the certifying bodies, but a 5% lower observed natural frequency than designed for, can significantly increase the endured fatigue loads due to dynamic amplification at the low-frequency wave spectrum. On the other hand, a higher measured natural frequency than designed for indicates an over-dimensioned, thus overpriced foundation design - or can facilitate design lifetime extension of the structure.

yielded $\zeta = 0.14\%$. Note that we thus assumed the dashpots to be frequency independent; although they were tuned based on the resonance peak at 5.4 Hz, we also used them for the lower frequency regime. For the soil resonator and the added soil mass models, the damping of the full structure would be $\zeta = 0.062\%$ and $\zeta = 0.054\%$, respectively. Damping identification (using Operational Modal Analyses, Stochastic Subspace Identification [14]) performed on the preliminary data retrieved from the full OWT structure in idling state, indicates 2 to 3% total logarithmic decrement support structure damping (often indicated with δ[3]), which gives $\zeta \approx 0.48\%$ damping ratio (of critical). The sum of the soil damping contribution based on the basic model ($\delta \approx \zeta(= 0.14\%) \times 2\pi = 0.88\%$ logarithmic decrement) and the assumed contributions (approximated for the current site conditions [9]) of the structural steel ($\delta \approx 1.2\%$), the water ($\delta \approx 0.5\%$, only 5m water depth) and air ($\delta \approx 0.5\%$ for idling, low wind velocity) lies in the expected range of 2 to 3% logarithmic decrement. The soil damping values retrieved with the soil resonator and soil added mass model seem too low. In general we can state that the soil damping contribution is quite low (even compared to values generally assumed in design), which is probably due to the very stiff soil at this location, limiting displacements and therefore energy dissipation. For this particular wind farm, this stiff-soil effect was taken into account in design; a similar low damping value was used in the simulations.

5.2.5. Soil nonlinearity

In the effective stiffness model we have assumed the soil to react in its linear-elastic regime - expecting that this is applicable for most of the occurring soil strains during operation of the OWT [24]. Clearly, in validating this model we have to assess whether indeed the soil reacted linearly for the actual displace-

[3] In the OWT industry, damping is often quantified in terms of the logarithmic decrement δ, which relates to the exponential decay between the maxima x_0 and x_n over n periods as $\delta = \frac{1}{n}\ln(\frac{x_0}{x_n})$. The relation between the damping ratio ζ and the logarithmic decrement is $\zeta = \frac{1}{\sqrt{1+(\frac{2\pi}{\delta})^2}}$. In practice, for small damping $\delta \ll 4\pi^2$, $\delta \approx 2\pi\zeta$.

ments during the shaker experiment. Figure 14 shows for example that the soil appears to have been excited (displaced) in its nonlinear regime for a part of the excitation frequencies. This can be concluded from the more or less parallel lines for the different weight setups in the optimized stiffness plot; the thick continuous blue and red lines of respectively the Middle weight and Heavy weight setups for frequencies between $\sim$2 Hz and 4 Hz, and the same blue line parallel to the thick continuous black line (Light weight) between 5 and 6.8 Hz, indicate a lower stiffness for a larger excitation force (displacement). Another indication of non-linearity is the slightly higher resonance frequency of 5.7 Hz observed in the transfer functions of the Light weight setup (Figure B.5) as opposed to the 5.4 Hz for the Middle weight setup. This could indicate a softening of the soil stiffness for larger applied forces.

The force - pile head displacement relation is often used to reflect the non-linearity of the SSI system. Figure 26 shows this relation for the calibrated shaker force (Equation 1, Table 1) and the measured displacements (retrieved from the accelerations in a similar way as in Equation 14), yielding a (model-independent) force-displacement relation for the pile-head. However, note that this is a *dynamic* force displacement relation; the inertial effects are included in these displacements. The excitation frequencies are noted next to the measurement points.

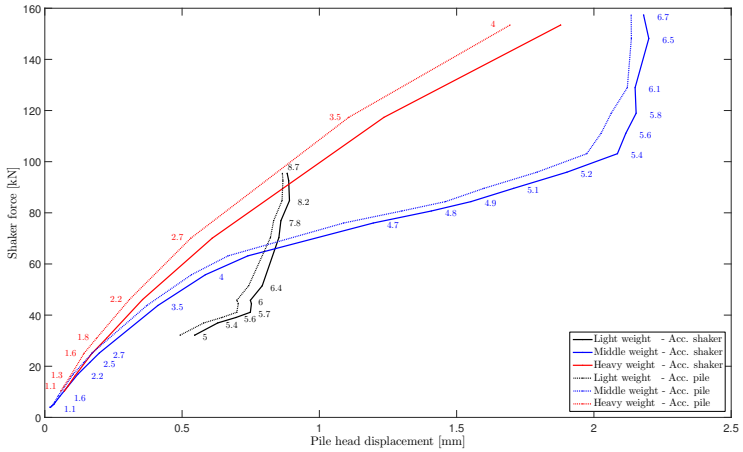

Figure 26: Shaker force - pile head displacement relations (at various frequencies) for the three different weight setups. The displacements were retrieved from the accelerometers attached to the pile and shaker. This can be considered a dynamic stiffness relation, as it includes inertial forces. The increase of dynamic stiffness for frequencies higher than 5.4 Hz is also clearly visible (blue and black lines).

To derive the more classical pile head stiffness, we corrected for these inertial effects by considering the displacements with respect to the sum of the external (shaker) and internal (inertial) forces. To derive the total inertial force, we first determined the single-degree-of-freedom (SDOF) equivalent stiffness term for the top of the pile in our (calibrated) basic model for a low frequency; for $\omega \to 0$ and a unit forcing, this is equal to the real part of the inverse of the displacement. Subsequently, we determined the SDOF equivalent mass for the other frequencies ($\omega > 0$) by taking into account the previously found stiffness contribution in the obtained modelled displacements. Figure 27 shows the stiffness of the pile head: the sum of shaker and inertial forces in relation to the displacements. From this we conclude that a rather linear effective soil stiffness applies for most of the displacements.

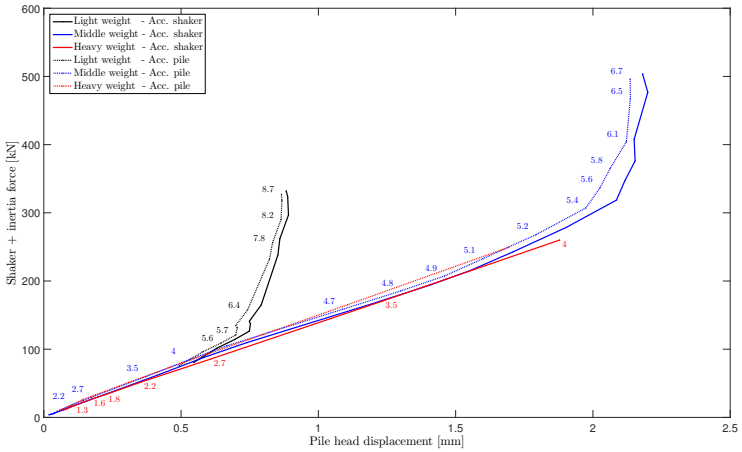

Figure 27: Sum of shaker and inertial force - pile head displacement relations for the three different weight setups. Initially, the relation is linear. The increase of stiffness for frequencies higher than 5.4 Hz is clearly visible (blue and black lines).

Both in Figures 26 and 27 the post-resonance (>5.4 Hz) stiffness increase can be clearly observed (indicated by the black and blue lines of respectively the Light and Middle weight setups). This stiffening is not necessarily related to a soil nonlinearity; although not verified at this stage, and while no pore-pressure build-up was observed [43] up to 4 Hz excitation (see also Appendix A), the stiffening beyond 5.4 Hz could be related to undrained behaviour of the soil.

Furthermore, we verified the soil strain in lateral direction (the direction of loading) in our static linear-elastic 3D model (Section 3) to be approximately $1 \cdot 10^{-6}$ for the shallowest 6 m of soil at a forcing of around 10 kN, corresponding to the Heavy weight setup exciting at 1 Hz. For a linear-elastic model, these numbers can be linearly scaled; a (static) force of 100 kN would induce strains in lateral direction in the order of $10 \cdot 10^{-6}$. Note however, that the strains predicted by the linear model can be underestimated. The often referred stiffness-strain degradation curve for sand of Atkinson & Sallfors [44] shown in Figure 28, indeed shows that for strains up to roughly $50 \cdot 10^{-6}$ the soil shear modulus only degrades with a small percentage.

Lastly, we check the embedded pile displacements of the (calibrated) basic model, for the forcing of the Middle weight setup at a frequency of 5.4 Hz. According to Figures 26 and 27 - these are the largest pile head deflections before the stiffening at higher frequencies are observed. The deflection at mudline is around 1 mm. This can be considered small; it is situated in the beginning of the initial linear branch of the associated p-y curve.

Concluding this discussion, we believe that - although not all observations are completely aligned - it is reasonable to assume linearly behaving soil in modelling the pile deflections during the shaker experiment.

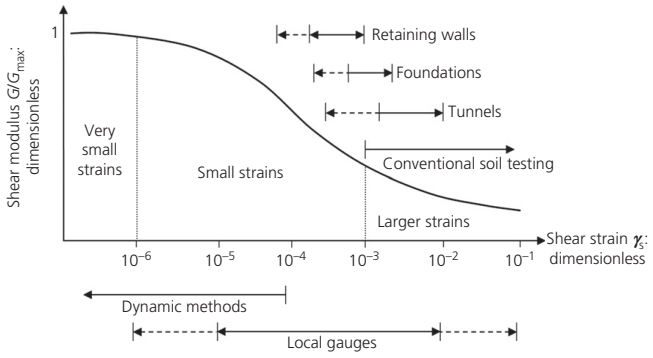

Figure 28: Typical stiffness - strain relation for sand [44].

6. Conclusions

In this paper we analyzed data obtained from a unique measurement setup; a monopile foundation in a near-shore wind farm was - prior to installation of tower and turbine - excited by an eccentric-mass shaker to assess the lateral dynamic (small-strain) stiffness of the pile. This data yielded a 'first-off' opportunity to validate a soil-structure interaction model for an in-situ rigidly behaving pile. With the controlled, known-input excitation - excluding aerody-

namic and super-structure disturbances - we determined the transfer and internal transmissibility functions between the strain gauges along the entire shaft of the pile and accelerometers attached to the top of the pile. A model-based identification was performed with a Timoshenko beam on Winkler foundation, of which the initial-guess stiffness profile $k_{eff}(z)$ was determined according to a previously published effective stiffness method for capturing the modulus of horizontal subgrade reaction for large-diameter piles [30].

Three tests with different eccentric weight setups were performed, at excitation frequencies ranging from 1.0 to 8.7 Hz. A frequency dependence of the stiffness is observed. The first resonance frequency of the soil-pile system appears to be situated around 5.4 Hz. The post-resonance response is characterized by an increase of the dynamic stiffness of the system. The effective stiffness profile $k_{eff}(z)$ was optimized to better match the measured response. Two modifications of the conventional 1D model were applied to assess whether the frequency dependency of the dynamic stiffness can be attributed to simple inertia effects. In the first modification, the observed resonance was assumed to be caused by the soil acting as a resonator, and in the second modification, the mass of the soil in the vicinity of the pile was added to the pile. Both these modifications lead to a rather constant soil-stiffness at frequencies up to the resonance regime. Based on the better match of the transfer and transmissibility functions, the basic model - including a frequency-dependent soil stiffness and possibly some added mass of the soil - is deemed most appropriate. Additionally, the damping contribution from the soil predicted by the basic model with the full OWT included, yielded the best agreement with the identified value.

Independent of the assumed 1D model, the low frequency-regime soil stiffness (relevant for OWTs) seems to be over-estimated by our effective stiffness (identified a priori using seismic cone penetration measurements and 3D modelling) with roughly 20%; including some added mass, a stiffness correction factor of 0.8 had to be applied to the effective stiffness profile $k_{eff}(z)$ to best match

the internal transmissibilities. This error, although not insignificant, is still small compared to the obtained mismatch when using the method prescribed by the design standards; a best estimate *p-y* stiffness profile under-estimates the observed stiffness for the low frequencies with a factor of 2.4 (140% under-estimation). Together with the fact that we see ample possibilities for improving our method in terms of the 3D model and 1D matching, this unique measurement setup has further improved our confidence in the validity of the developed stiffness method: a combination of in-situ seismic measurements, 3D modelling and 3D-1D translation.

Soil stiffness profiles that are in agreement with the (low-frequency) shaker measurements were used to predict the full OWT structure natural frequency using BHawC. Although these predictions come close to the identified (monitored) fundamental frequency, a slight over-prediction is observed. This difference could be related to identification or modelling errors, and could additionally be caused by the soil excavation and backfilling works that took place after the shaker measurements to pull in the electric cable. Furthermore, the sensitivity of the natural frequency of a stand-alone MP and a full OWT to the soil stiffness were discussed, arguing that the former is much more suitable for validating a soil model - especially for the ground conditions encountered at the site of investigation.

With the use of the basic model, the effective soil damping contribution for the pile-only situation is estimated to be around 20% damping ratio (of critical). Assuming frequency-independent damping coefficients, this damping contribution is estimated to result in a 0.14% damping ratio for the full structure including tower and RNA. Summed with commonly accepted values of the other damping contributions, this soil-pile damping is in agreement with the identified total damping ratio of 0.48%. This rather low damping could be related to the stiff character of the soil profile, leading to small displacements. Finally, we found the assumption of linear-elastic soil reactions for frequencies lower than

the resonance frequency to be acceptable.

In this contribution, a novel test setup for rigidly behaving, real-sized piles was presented in combination with an interpretation method that is suitable for analyzing forced vibrations of a highly damped system. The damping for the extended structure was shown to be in line with the value assumed in design, however the stiffness was shown to be underestimated by the design standards. In the model-based identification, we showed that our effective stiffness method yields a significantly higher accuracy in predicting the pile displacements than the p-y stiffness approach. The here presented interpretation of the experiment should be considered a first exploration; the data is expected to yield many more future insights into the complex SSI of rigidly behaving piles.

7. Acknowledgement

The work is part of the "DISSTINCT" project - a 4-year research project of Siemens Wind Power, Fugro, Delft University of Technology and DNV-GL aimed at improved dynamic soil characterization and modelling for offshore wind turbines [45], [46]. The DISSTINCT project is partly funded by the Dutch government (project number TKIW02001), for which the authors would like to express their gratitude. We would also like to thank Westermeerwind (the owner of the wind farm) and Van Oord (foundation designer and installation contractor) for their cooperation, Robin Greeuw for his valuable contribution in calibrating the shaker, and Hendrik Kramers for his full OWT identification analyses.

Appendix A. Geophysical characterization

This appendix contains supplementary information regarding the geophysical site characterization of which the output is given in Section 2.

The SCPT that was performed at location W27 reached a depth of 30 m (position of deepest geophone). A dual-phone cone was used with 0.5 m vertical spacing between the geophones. Multiple shots of the shear-wave hammer (placed at the mudline) were stacked per 1 m depth interval, resulting in a good quality of the data. In the identification of the shear-wave velocities we therefore used a 1 m layer thickness in discretizing the soil into homogeneous layers; the two geophones of each shot are placed in the middle of each assumed layer. In determining the interval times (the time lag between the arrival of the shear wave at the lower and upper geophone) and the associated shear-wave velocities C_s, we used the approach as described in [30], in which the C_s inversion was performed for a different position in the same wind farm. Here, we will only discuss the results and refer to [30] for details of the method.

The seismogram of the SCPT is shown in Figure A.1, and from a first glance we can already see some correspondence to the geotechnical profiles; a shallow clay and peat layer, situated at about 2-3 m depth causes the wave patterns recorded at these depths to be distorted. Due to this deviating pattern, we have to be cautious in cross-correlating these signals when determining the time lags.

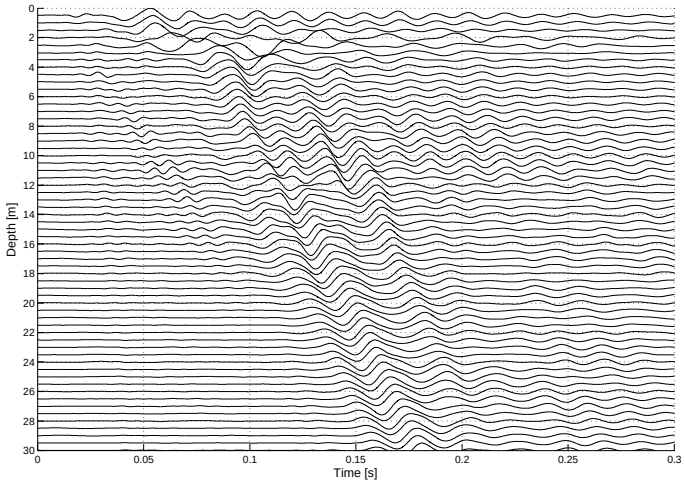

Figure A.1: Seismogram shot at W27

The resulting shear-wave profile is given in Figure A.2, in which, for comparison, also the tip resistance of the cone q_c (red line, see also the CPT output in Figure A.3) and the laboratory soil sample characterization are shown. The C_s and q_c profiles show similarities, but also some differences. This is most likely caused by the fundamentally different method: the large-strain, local and precise CPT versus the more small-strain (dynamic), global and averaged SCPT. The presence of the soft layer at a depth of about 20 m which is visible in the geotechnical output, Figures 2 and A.2, is less pronounced in the geophysical output. The clay layer is probably thin, stiff and confined enough to not cause any significant decrease of C_s at this depth.

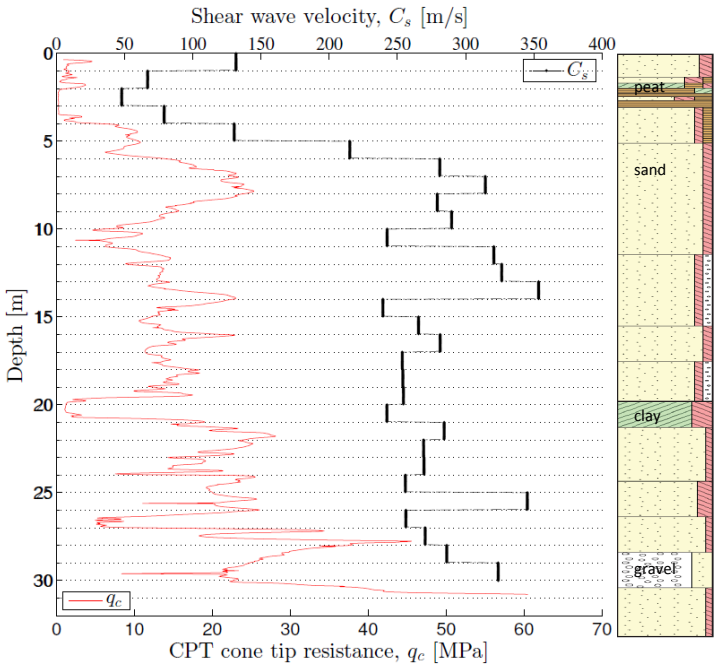

Figure A.2: Comparison of identified C_s profile ($\cdot - \bullet - \cdot$), cone tip resistance q_c ($-$), and borehole soil sample characterization from the laboratory (right side legend, the hatched pink colouring indicates the degree of silt in the samples).

With the determined profile for C_s and in-situ density ρ, we can readily calculate the shear modulus G. Also the Young's modulus E can be derived using an estimate of the Poisson's ratio ν of the layers:

$$C_s = \sqrt{\frac{E}{2(1+\nu)\rho}} = \sqrt{\frac{G}{\rho}}. \tag{A.1}$$

It is in general quite challenging to determine the magnitude of the soil's Poisson's ratio. In-situ permeability tests and an initial study indicating no pore-pressure build-up up to 4 Hz excitation [43], suggest that the soil profile has a large drainage capacity. We therefore estimate a relatively low Poisson's ratio for this saturated soil: $\nu = 0.25$ in case of a sand layer, $\nu = 0.40$ in case of a clay layer, and $\nu = 0.43$ in case of a peat layer. Nonetheless, we have previously shown that the Poisson's ratio - if chosen well below the incompressibility limit

of 0.5 - has minor influence on the pile displacement [30]. The first 1 m soil layer is assumed to behave less stiff in SSI than suggested by the C_s profile in Figure A.2 (130 m/s). This crust layer is likely to be affected by the pile driving. Therefore, the Young's modulus of this layer is assumed to have 50% of the value that is computed using Equation A.1. This is roughly equivalent to assuming 0.5 m scour, as was assumed in the design of the pile. Figure 3 shows the estimated Poisson's profile and computed Young's modulus for location W27. Note that due to averaging over the layers, the Poisson's ratio can deviate with respect to the assumed values per type of soil.

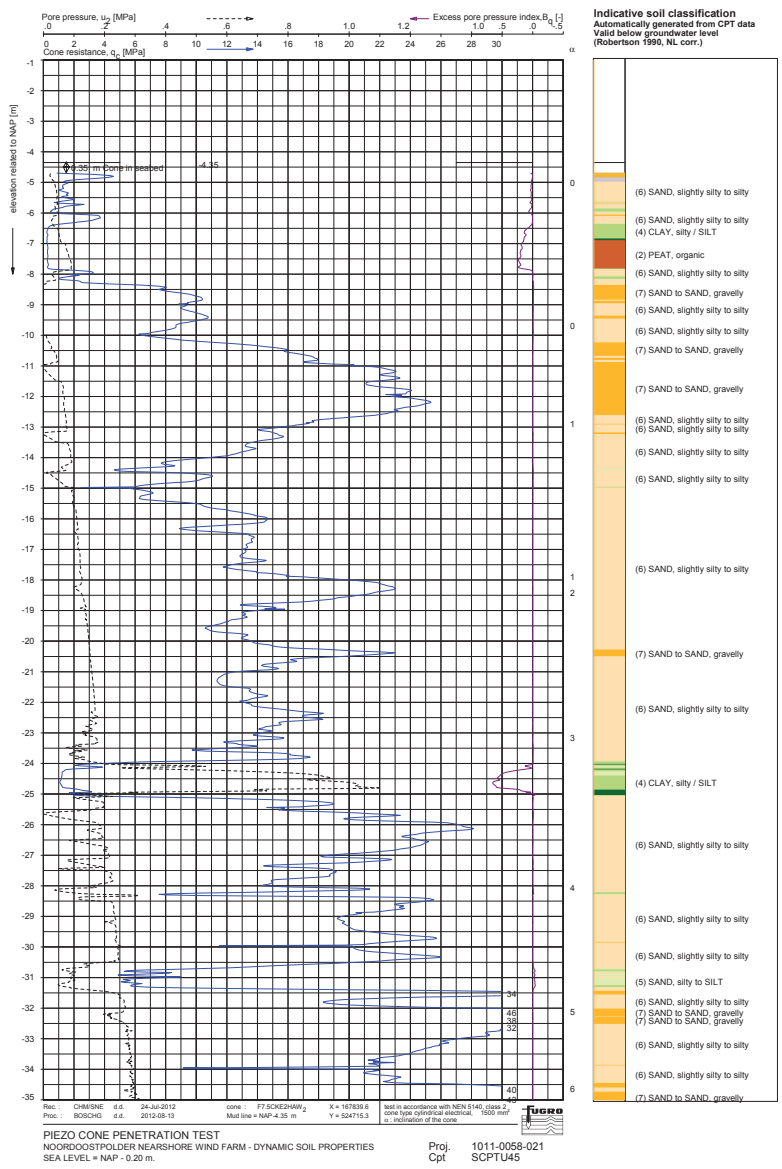

Figure A.3: CPT output (cone resistance q_c, pore pressure behind cone u_2, pore pressure index B_q and Robertson soil classification) from SCPT45 (location of turbine W27) measured in 2012. Note that the depth is given in relation to NAP, the Dutch equivalent of Mean Sea Level.

Appendix B. Data analysis - supplementary information

Figure B.1, showing an example of the steady-state (filtered) accelerometer response, is given as supplementary information to Section 4.

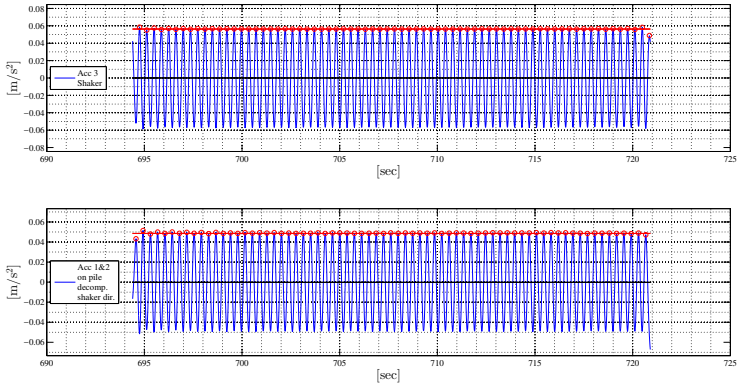

Figure B.1: Accelerometer responses after filtering for frequency plateau 2.68 Hz, Middle weight setup. The red circles indicate the picked peaks, of which the mean was taken over the selected cycles (red line). The signals of accelerometers 1 and 2, which were attached to the pile at 0.95 m below the shaker accelerometer (nr. 3), were combined to get the decomposed signal in the direction of the shaker excitation.

Table B.1 lists the used model parameters, which, together with the values given for the point masses, dashpot tuning coefficients α and stiffness correction factors γ listed in Section 5, are given for the purpose of repeatability of some of the presented results in this paper.

Symbol	Description	Value	Symbol	Description	Value
t	pile wall thickness [mm]	50	κ	Timoshenko shear coefficient [-]	0.53
E	Young's modulus steel [N/m^2]	$2.10 \cdot 10^{11}$	ρ	mass density steel [kg/m^3]	7850
G	shear modulus steel [N/m^2]	$8.08 \cdot 10^{10}$	$\rho_{s.plug}$	mass density soil plug [kg/m^3]	1500
D	diameter [m]	5	η	added soil mass factor [-]	3.4
L	embedded length [m]	24	M_s	soil resonator mass factor [-]	8.6
k_{eff} **pol.**	4th order polynomial values for k_{eff}, z=0..24 m	$9.3757 \cdot 10^5$, $-1.0308 \cdot 10^7$, $7.4008 \cdot 10^6$, $1.1771 \cdot 10^8$, $1.3055 \cdot 10^8$			

Table B.1: Model parameters. The top 4 and lowest 2 m of the pile have a 60 mm wall thickness for pile driving purposes.

Figures B.2, B.3 and B.4, showing examples of modelled and measured strains, are given as supplementary information to Section 5.1.1. The mismatch for the strains at higher frequencies between 10 and 15 m below mudline (shown in Figures B.3 and B.4) are apparent. This is related to an incorrect modelling of the inertia (or stiffness) at that location.

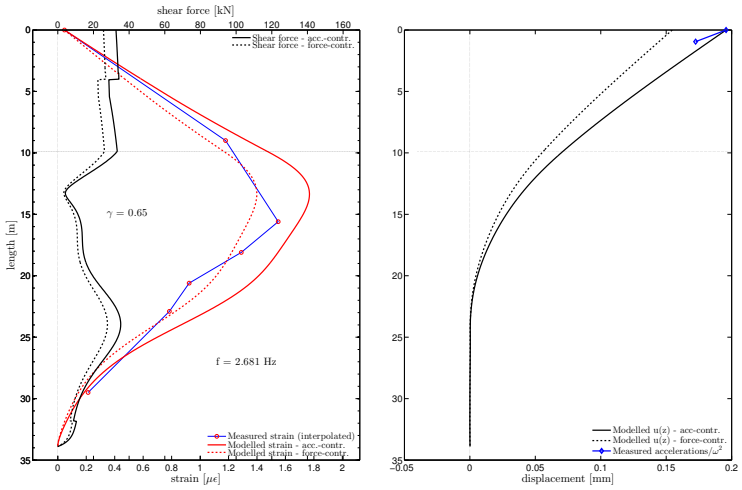

Figure B.2: Match in strains with a stiffness correction factor retrieved by optimizing for the internal transmissibility (Figure 14), for the Middle weight setup, exciting at a frequency of 2.68 Hz. The absolute values of both the acceleration- and force- controlled modelled responses are shown in terms of shear force and strain (left panel) and displacements (right panel).

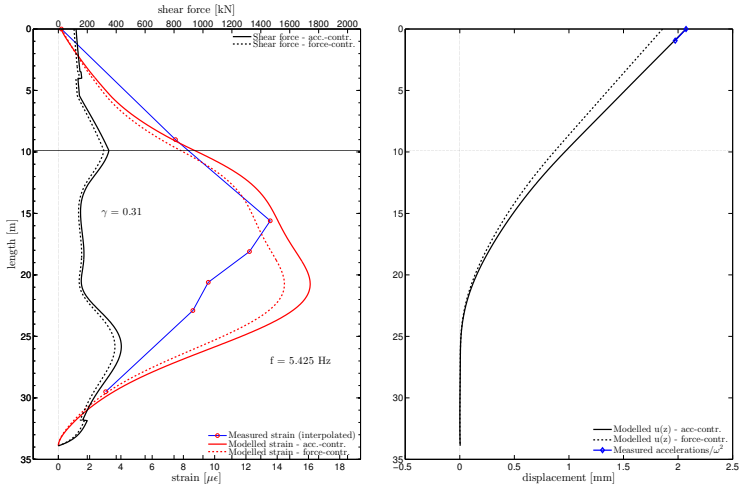

Figure B.3: Match in strains with a stiffness correction factor retrieved by optimizing for the internal transmissibility (Figure 14), for the Middle weight setup, exciting at a frequency of 5.42 Hz (resonance frequency). The absolute values of both the acceleration- and force-controlled modelled responses are shown in terms of shear force and strain (left panel) and displacements (right panel).

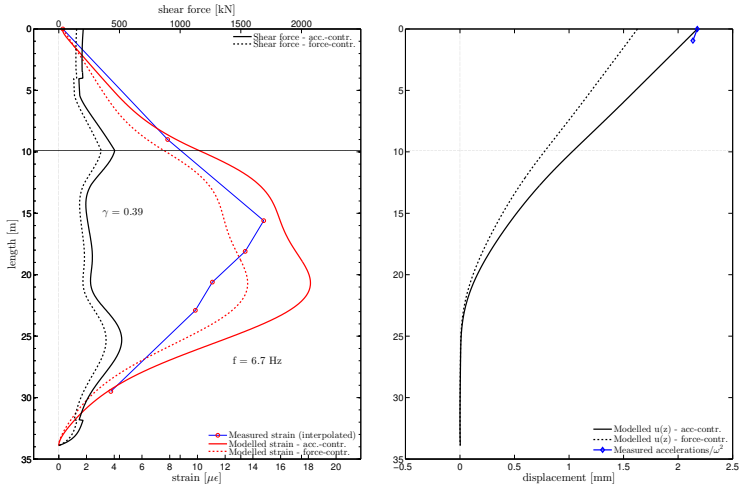

Figure B.4: Match in strains with a stiffness correction factor retrieved by optimizing for the internal transmissibility (Figure 14), for the Middle weight setup, exciting at a frequency of 6.70 Hz. The absolute values of both the acceleration- and force- controlled modelled responses are shown in terms of shear force and strain (left panel) and displacements (right panel).

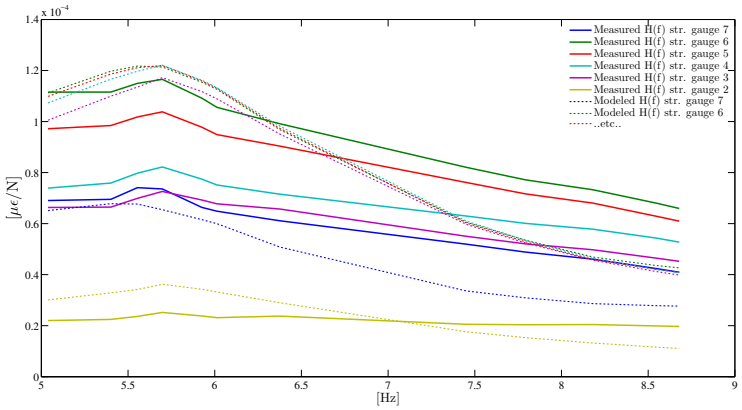

Figure B.5: Measured (continuous lines) and modeled (dotted lines) transfer functions for the strain gauges along the pile for the Light weight setup. For the modeled response, the factors on stiffness as given by the thick black line given in Figure 14 (optimization for transmissibilities: Equation 17) were applied to the effective 1D soil stiffness profile retrieved in Section 3. The dashpot coefficients were tuned for the transfer functions of the Middle weight setup (Figure 16) to a value of $c(z) = 1.56e^{-2}k_{eff}(z)$. As can be seen, the resonance peak has shifted from 5.4Hz (Middle weight setup) to 5.7Hz for this Light weight setup.

References

[1] D. Kallehave, B. W. Byrne, C. L. Thilsted, K. K. Mikkelsen, Optimization of monopiles for offshore wind turbines, Philos. Tr. Roy. S.-A 373 (2035) (2015) 20140100.

[2] L. C. Reese, W. R. Cox, F. D. Koop, Analysis of laterally loaded piles in sand, Proceedings of the 6th Annual Offshore Technology Conference, Houston, Texas, USA, (OTC 2080) (1974) 473–484.

[3] H. Matlock, Correlations for design of laterally loaded piles in soft clay, in: Offshore Technology in Civil Engineering: Hall of Fame Papers from the Early Years, ASCE, 1970, pp. 77–94.

[4] M. W. O'Neill, J. M. Murchinson, Fan Evaluation of p-y Relationships in Sands, Tech. rep., A report to the American Petroleum Institute (1983).

[5] C. L. Bakmar, Design of Offshore Wind Turbine Support Structures: Selected topics in the field of geotechnical engineering, Ph.D. thesis, Department of Civil Engineering, Aalborg University (2009).

[6] H. L. Davidson, Laterally loaded drilled pier research, Tech. rep., vol 1: Design Methodology, Vol. 2: Research Documentation, Final report by GAI Consultants Inc., to Electric Power Research Institute (EPRI) (1982).

[7] I. P. Lam, G. R. Martin, Seismic design for highway bridge foundations, in: Lifeline Earthquake Engineering: Performance, Design and Construction, ASCE, 1986, p. 21.

[8] Varun, D. Assimaki, G. Gazetas, A simplified model for lateral response of large diameter caisson foundations - linear elastic formulation, Soil Dyn. Earthq. Eng. 29 (2) (2009) 268–291.

[9] N. J. Tarp-Johansen, L. Andersen, E. D. Christensen, C. Mørch, S. Frandsen, B. Kallesøe, Comparing sources of damping of cross-wind motion, in:

European Offshore Wind 2009: Conference & Exhibition, The European Wind Energy Association, 2009.

[10] W. G. Versteijlen, A. V. Metrikine, J. S. Hoving, E. Smid, W. E. de Vries, Estimation of the vibration decrement of an offshore wind turbine support structure caused by its interaction with soil, in: Proceedings of the EWEA Offshore 2011 Conference, Amsterdam, The Netherlands, European Wind Energy Association, 2011.

[11] O. Rhersellah, Validity of identified modal parameters based on rotor-stop tests of offshore wind turbines (2013).

[12] M. Damgaard, L. B. Ibsen, L. V. Andersen, J. K. F. Andersen, Cross-wind modal properties of offshore wind turbines identified by full scale testing, Journal of Wind Engineering and Industrial Aerodynamics 116 (2013) 94–108.

[13] P. L. C. van der Valk, M. G. L. Ogno, Identifying Structural Parameters of an Idling Offshore Wind Turbine Using Operational Modal Analysis, in: F. N. Catbas (Ed.), Dynamics of Civil Structures, Volume 4, Conference Proceedings of the Society for Experimental Mechanics Series, Springer International Publishing, 2014, pp. 271–281. doi:10.1007/978-3-319-04546-7_31.

[14] H. C. Kramers, P. L. C. van der Valk, J. W. van Wingerden, Statistical evaluation of the identified structural parameters of an idling offshore wind turbine, in: Journal of Physics: Conference Series, Vol. 753, IOP Publishing, 2016, p. 052006.
URL http://stacks.iop.org/1742-6596/753/i=5/a=052006

[15] W. Weijtjens, R. Shirzadeh, G. De Sitter, C. Devriendt, Classifying Resonant Frequencies and Damping Values of an Offshore Wind Turbine on a Monopile Foundation for Different Operational Conditions, Ewea 2014 (2014) 83–87doi:10.1049/iet-rpg.2013.0229.

[16] C. Koukoura, A. Natarajan, A. Vesth, Identification of support structure damping of a full scale offshore wind turbine in normal operation, Renewable Energy 81 (2015) 882–895. doi:10.1016/j.renene.2015.03.079.

[17] G. Gazetas, R. Dobry, Horizontal Response of Piles in Layered Soils, J. Geotech. Eng. 110 (1) (1984) 20–40. doi:10.1061/(ASCE)0733-9410(1984)110:1(20).

[18] D. Badoni, N. Makris, Nonlinear response of single piles under lateral inertial and seismic loads, Soil Dynamics and Earthquake Engineering 15 (1) (1996) 29–43. doi:10.1016/0267-7261(95)00027-5.

[19] T. Nogami, M. Novak, Resistance of soil to a horizontally vibrating pile, Earthquake Engineering & Structural Dynamics 5 (3) (1977) 249–261. doi:10.1002/eqe.4290050304.

[20] M. Novak, T. Nogami, Soil-pile interaction in horizontal vibration, Earthquake Engineering & Structural Dynamics 5 (1977) 263–281. doi:10.1002/eqe.4290050305.

[21] L. M. Kagawa, Takaaki and Kraft, Dynamic characteristics of lateral load-deflection relationships of flexible piles, Earthq. Eng. Struct. Dyn. 9 (1) (1981) 53–68. doi:10.1002/eqe.4290090105.

[22] S. Corciulo, O. Zanoli, F. Pisanó, Transient response of offshore wind turbines on monopiles in sand: role of cyclic hydro–mechanical soil behaviour, Computers and Geotechnics 83 (2017) 221–238.

[23] M. Bayat, L. V. Andersen, L. B. Ibsen, p-y-$\dot{y}$ curves for dynamic analysis of offshore wind turbine monopile foundations, Soil Dyn Earthq Eng 90 (2016) 38–51.

[24] M. Damgaard, V. Zania, L. V. Andersen, L. B. Ibsen, Effects of soil-structure interaction on real time dynamic response of offshore wind turbines on monopiles, Engineering Structures 75 (2014) 388–401. doi:10.1016/j.engstruct.2014.06.006.

[25] W. G. Versteijlen, K. N. van Dalen, A. V. Metrikine, L. Hamre, Assessing the small-strain soil stiffness for offshore wind turbines based on in situ seismic measurements, in: J. Phys. Conf. Ser., Vol. 524, IOP Publishing, 2014, p. 012088. doi:10.1088/1742-6596/524/1/012088.

[26] G. W. Blaney, M. W. O'Neill, Measured lateral response of mass on single pile in clay, Journal of geotechnical engineering 112 (4) (1986) 443–457.

[27] C. B. Crouse, S. L. Kramer, R. Mitchell, B. Hushmand, Dynamic tests of pipe pile in saturated peat, Journal of geotechnical engineering 119 (10) (1993) 1550–1567.

[28] R. Osgood, G. Bir, H. Mutha, B. Peeters, M. Luczak, G. Sablon, Full-scale modal wind turbine tests: comparing shaker excitation with wind excitation, in: Structural Dynamics and Renewable Energy, Volume 1, Springer, 2011, pp. 113–124.

[29] B. Byrne, R. McAdam, H. Burd, G. Houlsby, C. Martin, K. Gavin, P. Doherty, D. Igoe, L. Zdravković, D. Taborda, et al., Field testing of large diameter piles under lateral loading for offshore wind applications, in: Proceedings of the 16th European Conference on Soil Mechanics and Geotechnical Engineering, Edinburgh, UK, 2015.

[30] W. G. Versteijlen, A. V. Metrikine, K. N. van Dalen, A method for identification of an effective Winkler foundation for large-diameter offshore wind turbine support structures based on in-situ measured small-strain soil response and 3D modelling, Engineering Structures 124 (2016) 221–236. doi:10.1016/j.engstruct.2016.06.007.

[31] K. Terzaghi, Evaluation of coefficients of subgrade reaction, Geotechnique 5 (4) (1955) 297–326.

[32] M. Jamiolkowski, D. C. F. Lo Presti, M. Manassero, Evaluation of relative density and shear strength of sands from cpt and dmt, in: Soil behavior and soft ground construction, ASCE, 2003, pp. 201–238.

[33] American Petroleum Institute (API), Recommended Practice for Planning, Designing and Constructing Fixed Offshore Platforms-Working Stress Design (RP 2A-WSD) (2000).

[34] R. Greeuw, Preliminary analysis of experimental data in offshore shaker tests, Tech. rep., Delft University of Technology, internship report (2016).

[35] F. W. Renting, K. N. van Dalen, A. V. Metrikine, Exact analytical expression for the added mass for offshore monopile foundations, In Preparation.

[36] K. F. Graff, Wave Motion in Elastic Solids, Oxford University Press, 1975.

[37] A. K. Chopra, Dynamics of Structures: Theory and Applications to Earthquake Engineering. (2007).

[38] A. Verruijt, An Introduction to Soil Dynamics, volume 24 of Theory and Applications of Transport in Porous Media (2010).

[39] J. K. Lim, B. Lehane, Interpretation difficulties of pile set-up in sand, in: Frontiers in Offshore Geotechnics III, CRC Press, 2015.

[40] F. Dezi, F. Gara, D. Roia, Dynamic response of a near-shore pile to lateral impact load, Soil Dyn Earthq Eng 40 (2012) 34–47.

[41] V. E. Komurka, A. B. Wagner, T. B. Edil, Estimating soil/pile set-up, Tech. rep., Wisconsin Highway Research Program (2003).

[42] M. Gerrits, A study on the natural frequency discrepancies in offshore wind turbines, Tech. rep., Delft University of Technology, internship report (2015).

[43] K. Pozorska, Investigation of the results of soil mechanics sensors at the shaker test on monopile W27 in the wind farm Westermeerwind in The Netherlands (2015).

[44] J. H. Atkinson, G. Sallfors, Experimental determination of stress-strain-time characteristic in laboratory and in situ tests, in: B. A A (Ed.), X

ECSMFE, Vol. III, Firenze Associazione Geotecnica Italiana, Italy, 1991, pp. 915–956.

[45] W. G. Versteijlen, S. N. Voormeeren, Efficient support structure design through improved dynamic soil structure interaction modeling, Tech. rep., TKI-WoZ Project Description, DISSTINCT (2013).

[46] TKI Wind op Zee DSSI project (DISSTINCT), `http://tki-windopzee.nl/project/dssi`, accessed: 2016-08-10.